Invited Feature Article

Charge transport in nanostructured materials for solar energy conversion studied by time-resolved terahertz spectroscopy

Hynek Němec [a,*], Petr Kužel [a], Villy Sundström [b]

[a] Institute of Physics, Academy of Sciences of the Czech Republic, 182 21 Prague, Czech Republic
[b] Department of Chemical Physics, Lund University, Getingevägen 60, 221 00 Lund, Sweden

ARTICLE INFO

ABSTRACT

Spectra of far-infrared conductivity contain useful information on charge transport at nanoscopic length scales. However, decrypting the mechanisms and parameters of charge transport from the measured spectra is a complex task in nanostructured systems: in particular, the conductivity is strongly influenced by charge carrier interaction with surfaces or interfaces between constituents of the composite material as well as by local field effects. Here we review our work on transient far-infrared conductivity in polymer:fullerene bulk heterojunctions and in bare and dye-sensitized semiconductor nanoparticles. Measurements performed by time-resolved terahertz spectroscopy are complemented by Monte-Carlo calculations which clearly link the charge transport properties and the terahertz conductivity spectra.

© 2010 Elsevier B.V. All rights reserved.

1. Introduction

A large effort is currently devoted to replace many devices made of bulk inorganic semiconductors by those produced by energetically and economically more favorable thin film technologies and nanotechnologies. This tendency is particularly important for the development of photovoltaic cells for solar energy conversion into electricity. The most widespread cells are based on crystalline and multi-crystalline silicon and they can reach efficiencies of 25% and 20%, respectively [1], but the production is rather expensive since melting of a large amount of material is required in the elaboration process. Power conversion efficiency of Grätzel and plastic (bulk heterojunction, BHJ) solar cells, for example, is still considerably lower (values of 11.2% and 7.9% have been reported recently [1] for BHJ cells and Grätzel cells, respectively); on the other hand, the possibility to employ inkjet printing and thin film technologies for their fabrication may significantly reduce the costs.

The power conversion efficiency of photovoltaic cells is controlled by several factors, which include light harvesting efficiency, charge generation, recombination, separation and transport to electrodes and energetics of the active materials. The common property of most of the thin-film-based devices is a large complexity related to the lack of long-range order. For example, both intra- and inter-chain transport has to be considered in bulk heterojunctions. Due to the large disorder inherent to these materials, a high density of non-conducting states and defect levels exists and for this reason, the long-range charge transport is slowed down. The charge transport is thus a serious issue in the thin film devices: it must be fast enough in order to avoid the charge recombination. In such a case, the internal conversion efficiency may reach 100%, as it has been demonstrated recently in a bulk heterojunction [2].

The mechanisms of charge transport in solar cell materials are frequently investigated using time-of-flight methods or in a field-effect transistor configuration [3]. These methods indeed provide detailed information on long-range charge transport which is highly pertinent for the device operation. The long-range transport can be limited by inefficient inter-chain or inter-nanoparticle transport to a large extent. Optimization of elaboration technologies (e.g. by self-assembling polymer chains in bulk heterojunctions [4] or by fabricating semiconductor nanorods instead of nanoparticles [5–7]) may overcome this bottleneck and the overall transport would be then controlled by the short-range mobility. However, due to the apparent experimental difficulties, very little is known about the mobility in individual nano-elements.

Time-resolved terahertz (THz) spectroscopy is a non-contact technique for conductivity measurement with sub-picosecond time resolution and using low electric fields (kV/cm) [8,9]. Due to the high frequency of THz electric field, the method probes the

* Corresponding author at: Institute of Physics, Academy of Sciences of the Czech Republic, Na Slovance 2, 18221 Prague, Czech Republic. Tel.: +420 266 052 953; fax: +420 286 890 415.
   E-mail address: nemec@fzu.cz (H. Němec).

transport on a length scale of units to hundreds of nanometers [10,11]. This is precisely the scale of short-range transport in bulk heterojunctions and in semiconductor nanoparticles. The time resolution makes it possible to bring new insight into the dynamics early after photoexcitation.

In many aspects, time-resolved THz spectroscopy provides unique information, which cannot be obtained by other methods. All-optical pump–probe methods offer an excellent time resolution, but they are only sensitive to the occupation of the probed states. Though the free-carrier absorption tail can be detected using longer probing wavelength, it does not contain any fingerprints of the charge transport mechanisms. The transport mechanisms can be studied using time-of-flight or time-resolved microwave conductivity techniques, but the time resolution is usually not better than nanoseconds [12]. Sub-picosecond time resolution and sensitivity to the transport properties achievable in transient Stark spectroscopy is paid off by the necessity to apply very high electric fields (MV/cm) which often fundamentally affect the charge mobility [13].

In the past, time-resolved THz spectroscopy has been employed for the investigation of various bulk inorganic semiconductors, with a certain emphasis to characterize ultrafast materials with high mobility [14,15]. The response of conduction band charge carriers can be well described and straightforwardly understood in terms of the Drude formula for the response of free charge carriers (Fig. 1a) which describes the conductivity over many frequency decades. Despite the presence of conduction band charge carriers in semiconductor nanoparticles and bulk heterojunctions, their THz conductivity spectra completely differ from the bulk picture (Fig. 1b). A thorough understanding of these spectra is still a subject of intensive research.

The main aim of this paper is to provide a coherent interpretation of the mobility and conductivity in organic bulk heterojunctions (BHJ) and in nanostructured (dye-sensitized metal oxide) semiconductors. The paper is organized as follows. In Section 2, we present the basic phenomenological models which are commonly used for the interpretation of the far-infrared spectra. The investigated systems are inhomogeneous, and therefore their effective (averaged) response can markedly differ from the response of their constituents due to the presence of depolarization fields. Impact of the depolarization fields is described using an effective medium approximation in Section 3. Section 4 is devoted to an overview of experimental work on organic semiconductors and semiconductor nanostructures. In Section 5 we show microscopic models which have been developed for the interpretation of THz conductivity spectra in various nanostructured model systems. Two systems are then investigated thoroughly. Ultrafast dynamics in polymer:fullerene BHJ is discussed in detail in Section 6, whereas Section 7 presents some recent results on the photo-induced dynamics in dye-sensitized semiconductor nanoparticle films.

It should be noted that in this paper, we push forward the interpretations of the observed conductivity spectra. We intentionally skip details on the THz instrumentation, since there are excellent reviews on this subject [8,9,16].

2. Phenomenological models of the far-infrared response

The THz electric field interacts with electrons and ions of a material. The interaction strength for a given frequency f (or equivalently, angular frequency $\omega = 2\pi f$) is characterized by the (electric) conductivity spectrum $\sigma(f)$ and by the (dielectric) susceptibility spectrum $\chi(f)$, which, in equilibrium, are determined solely by the microscopic structure of the material. The conductivity is associated with the current of free charges while the susceptibility is associated with the polarization of bound charges. It is often convenient to ignore the difference between the real current of free and the polarization current of bound charges and to describe the response of material by a single *complex* response function by considering the equivalence

$$\sigma(f) \Leftrightarrow -2\pi i f \varepsilon_0 \chi(f), \tag{1}$$

where ε_0 is the permittivity of vacuum.

Upon photoexcitation, the properties of a material may be altered, i.e., the (complex) conductivity changes from $\sigma(f)$ to $\sigma(f) + \Delta\sigma(f)$, where the term $\Delta\sigma(f)$ is called the photo-induced or transient conductivity. Though the vast majority of the work discussed in this paper is related to the photo-induced conductivity, most of the conclusions apply to the equilibrium conductivity $\sigma(f)$ as well.

The conductivity normalized by the charge density en (n is the carrier density and e is the charge) gives an average mobility $\mu(f)$ per charge carrier. The frequency dependence of the mobility naturally originates from the fact that charge carriers may move with different velocity in electric fields oscillating at different frequencies. In optical pump–THz probe experiments the excitation fluence can be measured in order to determine the number of excitation events (absorbed photons) n_{exc} per laser pulse and per unit volume. However, the quantum yield ξ of photoexcited carriers is often unknown, therefore we cannot directly evaluate the carrier density $n = \xi n_{exc}$ and in turn, the carrier mobility $\mu(f)$. We thus normalize the transient conductivity $\Delta\sigma(f)$ by en_{exc} and the result represents the product of the quantum yield and carrier mobility:

$$\xi \times \mu(f) = \frac{\Delta\sigma(f)}{en_{exc}}. \tag{2}$$

This product is the essential output of experiments presented in the paper.

In most semiconductors photoexcitation generates free carriers. Within the semiconductor band structure, the carriers do not feel any potential and they are scattered by phonons, lattice defects, impurities, etc. The scattering process randomizes the carrier velocity. If the time between successive scattering events follows an exponential distribution with the average time τ_s, the mean velocity induced by a delta-pulse of electric field with strength E decays as

$$v(t) = \frac{eE}{m} \exp\left(\frac{-t}{\tau_s}\right), \tag{3}$$

where m is the effective mass of charge carriers. The mobility describes an ability of charge carriers to move in the electric field and its spectrum is thus defined as $\mu(\omega) = v(\omega)/E$. Calculating the Fourier transform $v(\omega)$ of Eq. (3), we get the classical Drude formula of the mobility spectrum of free charges:

$$\mu(\omega) = \frac{e\tau_s}{m} \cdot \frac{1}{1 - i\omega\tau_s}. \tag{4}$$

Eq. (4) expresses two general trends which are characteristic for the response of any charge carriers which do not exhibit any confinement, i.e., which can efficiently move over very long distances: the real part of the mobility monotonously decreases with increasing frequency whereas the imaginary part is always positive and it describes an inductive response (Fig. 2). In the Drude formula [Eq. (4)], the dc (zero frequency) mobility reaches the well-known value $e\tau_s/m$ and the imaginary part has a maximum at a frequency $1/(2\pi\tau_s)$. Since typical scattering times in bulk inorganic semiconductors at room temperature are of the order of tens to hundreds of femtoseconds, a substantial dispersion in the mobility spectra is expected at THz frequencies. Measurement of the shape of the conductivity spectrum thus constitutes a mean for scattering time determination [14,15,17].
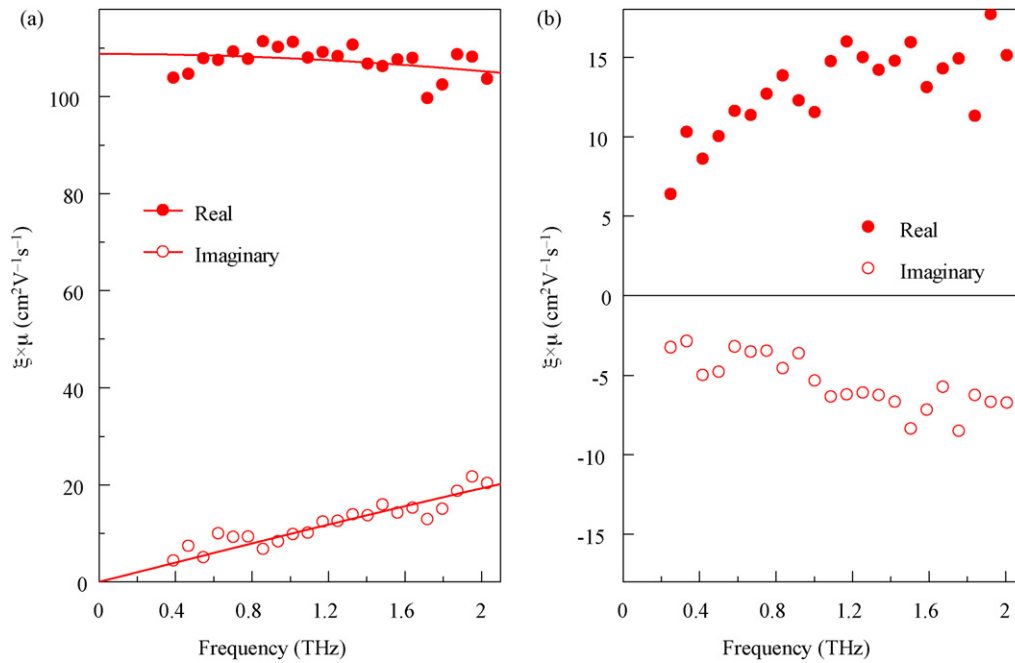
Fig. 1. Comparison of mobility spectra of photogenerated electrons measured in various forms of ZnO. (a) The spectrum of a ZnO single crystal shows a typical Drude response (solid line represents a fit with scattering time of 14 fs). (b) Mobility in ZnO nanoparticles is considerably lower and its spectrum (shape) is completely different.

Long-distance transport of charge carriers can be prohibited if there is a restoring force driving them back to their equilibrium position upon displacement. Such bound charges are found e.g. in excitons or in localized levels like traps. The small charge displacements x encountered with the usual strengths of the THz electric fields can be described in terms of a driven harmonic oscillator:

$$m\frac{d^2x}{dt^2} + m\gamma\frac{dx}{dt} + m\omega_0^2 x = eE(t), \tag{5}$$

where $f_0 = \omega_0/2\pi$ is the oscillator resonant frequency and γ is the oscillator damping rate. Fourier transformation of the charge velocity $v = dx/dt$ then leads to the mobility spectrum

$$\mu(\omega) = \frac{e}{m} \cdot \frac{-i\omega}{\omega_0^2 - \omega^2 - i\gamma\omega}. \tag{6}$$

The behavior of mobility below the resonant frequency is in a sharp contrast with the Drude model (4). Below f_0, the real part first quadratically increases from zero and it peaks at the resonant frequency f_0 whereas the imaginary part is negative – at the lowest frequencies it exhibits a linear decrease (a capacitive-type response) and after reaching a minimum, it crosses zero at f_0. A real part increasing with frequency and a negative imaginary part are
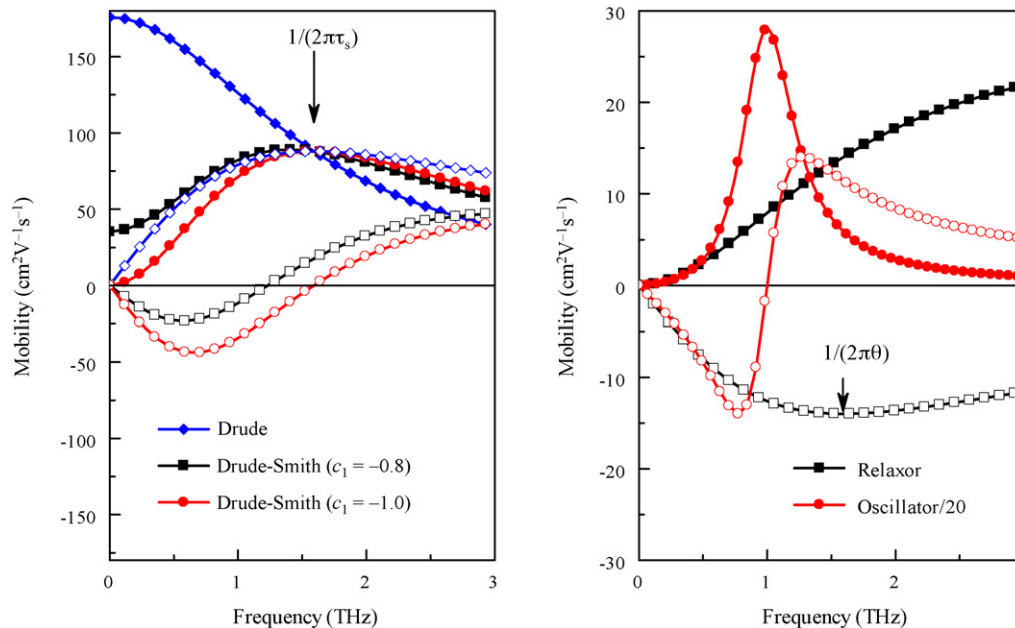
Fig. 2. Examples of mobility spectra corresponding to various phenomenological models. Closed symbols: real part, open symbols: imaginary part. Left panel: Drude and Drude–Smith model ($\tau_s = 100$ fs). Right panel: oscillator model [$f_0 = 1$ THz, $\gamma = 2\pi/(2$ ps)] and relaxation model [$\theta = 100$ fs, $\gamma = 2\pi/(100$ fs)]. The amplitude of the oscillator model is large due to the small damping and it was scaled down by a factor of 20. The mass m was always set equal to the mass of a free electron m_e.

typical signatures of carrier localization, not only within the harmonic approximation. Above f_0, the kinetic energy of carriers will dominate over the potential energy and the carrier motion will be limited by its inertia and not by the potential profile. Indeed, in the prototypic case of a harmonic oscillator above the resonant frequency, we can identify the behavior known from the Drude model (4): the real part decreases with frequency and the imaginary part is positive. In other words, for high-enough frequencies, charge carriers no longer feel the localization.

In the case of an overdamped oscillator ($\gamma \gg \omega_0$), the low-frequency mobility approaches

$$\mu(\omega) = \frac{e}{m\gamma} \cdot \frac{i\omega\theta}{i\omega\theta - 1}, \tag{7}$$

which expresses the response of a Debye relaxation with the relaxation time $\theta = \gamma/\omega_0^2$. Here the real part increases from zero and for frequencies $\omega \gg \theta$ it saturates at the value of $e/(m\gamma)$. The imaginary part is negative and peaks at the frequency $1/(2\pi\theta)$. Note that this expression is valid for low frequencies only. For higher frequencies, it does not reflect the increasing kinetic energy of carriers and therefore the real part does not drop to zero which violates the sum rule.

The conductivity of nanostructured systems is frequently fitted by an extension of the Drude formula proposed by Smith [18]. It is based on a Drude model with the consideration of possibly anisotropic scattering. The mobility spectrum reads

$$\mu(\omega) = \frac{e\tau_s}{m} \cdot \frac{1}{1 - i\omega\tau_s} \left[1 + \sum_{n=1}^{\infty} \frac{c_n}{(1 - i\omega\tau_s)^n} \right], \tag{8}$$

where the coefficients c_n describe the persistence of velocity in the nth scattering event and they can be identified with the mean cosine of the scattering angle: values lower than zero indicate a preferential back-scattering. If the collisions were independent, c_n would be equal to c_1^n. In such a case, the series can be summed up and it turns out that the result is the simple Drude model (4) with a modified relaxation time $\tau_s/(1 - c_1)$. Smith thus made an important assumption that the persistence of velocity is retained only in the first collision ($c_1 \neq 0$, $c_n = 0$ for $n \geq 2$) which reduces Eq. (8) to

$$\mu(\omega) = \frac{e\tau_s}{m} \cdot \frac{1}{1 - i\omega\tau_s} \left[1 + \frac{c_1}{1 - i\omega\tau_s} \right]. \tag{9}$$

This expression is often called the Drude–Smith model. On the one hand, the model (9) fits very well the conductivity spectra in a rich variety of systems, ranging from poor metals over semiconductor nanostructures to polymers [18–20]. Its universality is due to the possibility to change continuously the coefficient c_1 and thus to tune the response from delocalized ($c_1 = 0$) to localized ($c_1 = -1$). On the other hand, the model was criticized that it does not respect the time homogeneity, i.e. that the first scattering event is different from the others [21]. This makes the microscopic interpretation of the parameters of the Drude–Smith model ambiguous. In Section 5 we will review some recent microscopic models of the far-infrared transient conductivity of nanostructured systems. It will be shown that these models can be often approximated by the Drude–Smith model when a limited spectral range is considered, which allows establishing the microscopic meaning of the parameters of the Drude–Smith model. However, it will also be shown that the Drude–Smith model necessarily fails in systems possessing various localization length scales.

3. Local field effects

When dealing with strongly inhomogeneous systems, it is necessary to consider that the local electromagnetic field generally differs from the applied one due to the presence of depolarization fields. In this section, we evaluate the screening of the electric field of the THz pulse due to the dielectric structure of the system. This is a purely electromagnetic effect and it is in a sharp contrast with Section 5 where an influence of potential barriers on charge transport is described – these may be present even in a system which is dielectrically percolated. In other words, in Section 5 we evaluate the response of carrier to the local field (i.e., to the field at the place where the charge actually is); in this section, we determine this local field.

In nanostructured systems, the dimensions are typically smaller than 1 μm and they are thus much smaller than the wavelength of the probing radiation (>0.1 mm for frequencies below 3 THz). The problem of depolarization fields can be then best accounted for by a suitable effective medium approximation which relates the effective (measured) conductivity with the conductivity of the constituents. Choice of the effective medium model is determined by the material nanostructure. For example, Maxwell-Garnett theory [22] applies for diluted non-percolated particles dispersed in a matrix, whereas the Bruggeman model [23] can account for the percolation of particles.

The impact of depolarization fields on the conductivity spectra is best illustrated within the Maxwell-Garnett approximation where the effective properties can be expressed in a mathematically very simple form. The model assumes a mixture of sparse non-percolated particles embedded in a (percolated) matrix. Let us denote ε_p and $\Delta\sigma_p$ the permittivity and the transient conductivity, respectively, of the particles; ε_m and $\Delta\sigma_m$ the permittivity and the transient conductivity, respectively, of the matrix; and ε and $\Delta\sigma$ the effective permittivity and the transient conductivity, respectively, of the composite. We can thus straightforwardly analyze the cases where either the non-percolated component (particle) is photoconducting ($\Delta\sigma_p \neq 0$, $\Delta\sigma_m = 0$), or where the percolated component (matrix) is photoconducting ($\Delta\sigma_m \neq 0$, $\Delta\sigma_p = 0$).

In equilibrium, the Maxwell-Garnett model reads

$$\frac{\varepsilon - \varepsilon_m}{\varepsilon + K\varepsilon_m} = s \cdot \frac{\varepsilon_p - \varepsilon_m}{\varepsilon_p + K\varepsilon_m}, \tag{10}$$

where s is the volume fraction of the particles and K is the shape factor ($K = 2$ for spherical particles and $K = 1$ for cylinders with the axis perpendicular to the electric field polarization). The equilibrium effective permittivity ε can be simply expressed from Eq. (10):

$$\varepsilon = \varepsilon_m \cdot \frac{\varepsilon_p(1 + Ks) + \varepsilon_m(1 - s)}{\varepsilon_p(1 - s) + \varepsilon_m(s + K)}. \tag{11}$$

Eq. (10) can be straightforwardly generalized for the out-of-equilibrium case by replacing ε_j by $\varepsilon_j + i\Delta\sigma_j/(\omega\varepsilon_0)$:

$$\frac{\varepsilon + \frac{i\Delta\sigma}{\omega\varepsilon_0} - \left(\varepsilon_m + \frac{i\Delta\sigma_m}{\omega\varepsilon_0}\right)}{\varepsilon + \frac{i\Delta\sigma}{\omega\varepsilon_0} + K\left(\varepsilon_m + \frac{i\Delta\sigma_m}{\omega\varepsilon_0}\right)} = s \cdot \frac{\varepsilon_p + \frac{i\Delta\sigma_p}{\omega\varepsilon_0} - \left(\varepsilon_m + \frac{i\Delta\sigma_m}{\omega\varepsilon_0}\right)}{\varepsilon_p + \frac{i\Delta\sigma_p}{\omega\varepsilon_0} + K\left(\varepsilon_m + \frac{i\Delta\sigma_m}{\omega\varepsilon_0}\right)}. \tag{12}$$

We analyze Eq. (12) separately for cases when only the particles are conducting and when only the matrix is conducting.

For conducting particles in a non-conducting matrix ($\Delta\sigma_p \neq 0$, $\Delta\sigma_m = 0$), Eq. (12) simplifies to

$$\Delta\sigma = \Delta\sigma_p \cdot \frac{\varepsilon_m(1 + sK) - \varepsilon(1 - s)}{\varepsilon_m(s + K) + \varepsilon_p(1 - s) + \frac{i\Delta\sigma_p}{\omega\varepsilon_0}(1 - s)}. \tag{13}$$

Let us now examine how an increase of the transient conductivity of particles (e.g. by increasing the excitation density) affects the effective transient conductivity $\Delta\sigma$. For low excitation density, $\Delta\sigma_p$ is small and it can be neglected in the denominator, at least for higher frequencies ($|\Delta\sigma_p/\omega\varepsilon_0| \ll |\varepsilon_m|, |\varepsilon_p|$). In such a case, $\Delta\sigma \propto \Delta\sigma_p$ and the proportionality factor depends solely on the equilibrium permittivities ε_p and ε_m and on the structural parameters s and K. For high-enough excitation density, the $\Delta\sigma_p$ term in the denominator
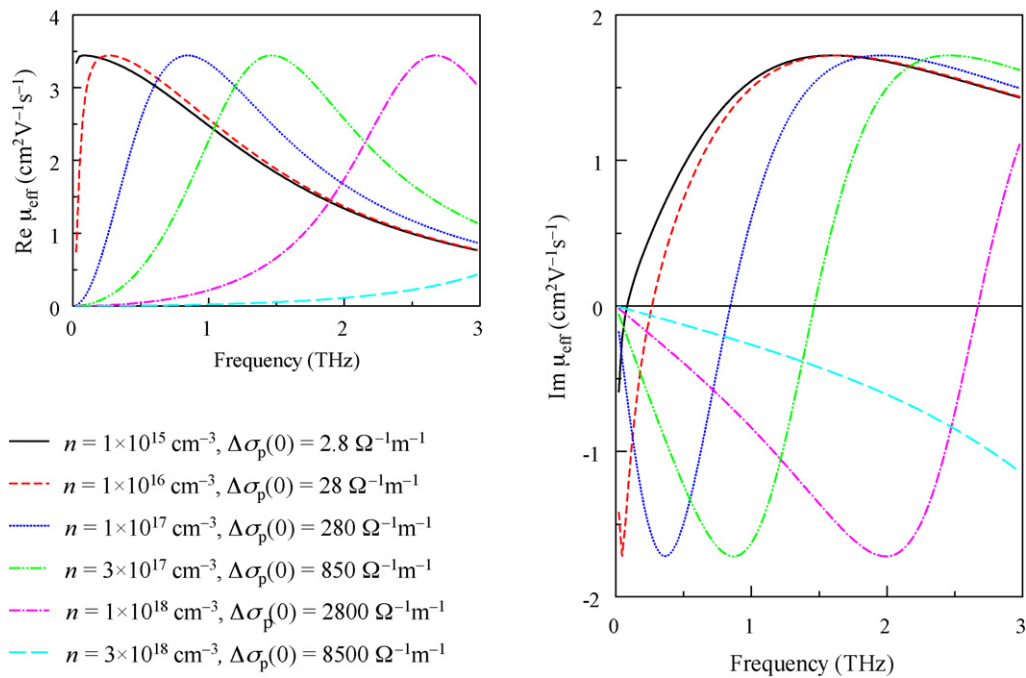
Fig. 3. Real and imaginary part of "effective" mobility [defined as $\mu_{eff} = \Delta\sigma/(ne)$] calculated within the Maxwell-Garnett theory (13) for various charge carrier densities n. Parameters used for the calculation were $K = 2$, $s = 0.1$, $\varepsilon_p = 7.8$, $\varepsilon_m = 1.5$, $\Delta\sigma_m = 0$, $\Delta\sigma_p = ne\mu_p$ where the mobility of charges inside the particles μ_p follows the Drude model (4) with the same parameters as in Fig. 2. The values of $\Delta\sigma_p$ at zero frequency are also indicated to provide an order of magnitude estimate of the conductivities where the local field effects start to change the spectral shape dramatically.

will dominate and the effective transient conductivity $\Delta\sigma$ (proportional to $-i\omega$) will no more depend on $\Delta\sigma_p$. These two regimes are characteristic for any structure containing non-percolated conducting particles embedded in a non-conducting matrix. For low excitation densities, the effective transient conductivity is simply proportional to the transient conductivity of the particles, while for high excitation density, the effective transient conductivity saturates and approaches a negative frequency-dependent imaginary value. This behavior is illustrated in Fig. 3, where we consider charges inside isolated particles with $\Delta\sigma_p$ exhibiting the Drude behavior. The particles conductivity $\Delta\sigma_p$ scales linearly with the density of charge carriers. For low carrier densities (and not too low frequencies), the effective conductivity $\Delta\sigma$ follows the Drude model as well. However, with increasing carrier density, the effective transient conductivity deviates from the Drude model and a resonant behavior clearly appears [24]. This so-called plasmonic resonance can be described by a harmonic oscillator response with specific amplitude and parameters f_0 and γ [21]. The essential difference with Eq. (6) is that here the resonant frequency f_0 varies with the excitation fluence.

For the opposite case of a conducting matrix containing non-conducting particles ($\Delta\sigma_m \neq 0$, $\Delta\sigma_p = 0$), Eq. (12) becomes

$$\Delta\sigma = \Delta\sigma_m \cdot \frac{\varepsilon_p(1 + sK) + \left(2\varepsilon_m + \frac{i\Delta\sigma_m}{\omega\varepsilon_0}\right)K(1-s) - \varepsilon(K+s)}{\varepsilon_p(1-s) + \left(\varepsilon_m + \frac{i\Delta\sigma_m}{\omega\varepsilon_0}\right)(K+s)}. \quad (14)$$

This equation greatly simplifies for the case prevailing in percolated nanocrystalline semiconductor films in which $\varepsilon_p \ll \varepsilon_m$ (for example, ZnO and TiO$_2$ matrices with air voids) and it reduces to $\Delta\sigma = \Delta\sigma_m \cdot K(1-s)/(K+s)$ independently of $\Delta\sigma_m$, which means that the spectra of transient effective conductivity and the transient conductivity of the matrix have identical shape and they differ only in amplitude.

For a low-permittivity matrix ($\varepsilon_p \gtrsim \varepsilon_m$), the behavior of Eq. (14) may be very complicated. For illustration, we point out a few properties for the case $\varepsilon_p \gg \varepsilon_m$. In the low $\Delta\sigma_m$ regime, the effective conductivity becomes $\Delta\sigma = \Delta\sigma_m \cdot (1 + sK)/(1-s) > \Delta\sigma_m$, which shows that $\Delta\sigma$ is enhanced due local fields induced by the high-permittivity particles. In the high $\Delta\sigma_m$ limit, we obtain $\Delta\sigma = \Delta\sigma_m \cdot K(1-s)/(K+s) < \Delta\sigma_m$. The transition between these regimes cannot be described in terms of variation of the proportionality constant and a substantial reshaping of the conductivity spectrum may occur at intermediate excitation densities.

The properties of Eqs. (13) and (14) allow us to draw important general conclusions for experiments with inhomogeneous systems where a dependence on the excitation density is measured. For low excitation densities ($|\Delta\sigma_j/(\omega\varepsilon_0)| \ll |\varepsilon_j|, j \in \{p, m\}$), the effective conductivity always follows the conductivity $\Delta\sigma_j$ of the conductive component ($j = m$ or p). If the effective conductivity remains proportional to $\Delta\sigma_j$ even for $|\Delta\sigma_j/(\omega\varepsilon_0)| \gtrsim |\varepsilon_j|$, it is possible to conclude that the conducting parts of the sample are mostly percolated (and to a certain extent confirm the assumption $\varepsilon_p \ll \varepsilon_m$). On the other hand, development of a resonance in the spectrum of $\Delta\sigma$ and its blue shift with increasing excitation fluence evidences that the conducting parts of the system are isolated from each other. Note however, that for high excitation fluences the spectrum of the conducting parts $\Delta\sigma_j$ may change as well. Care has thus to be taken to separate effects due to depolarization fields and due to the intensity-dependence of the intrinsic conductivities $\Delta\sigma_p$ or $\Delta\sigma_m$.

In experiments, the pump beam is often absorbed only near the surface of the investigated sample and the transient conductivities $\Delta\sigma_p$ and $\Delta\sigma_m$ then decrease exponentially with the depth of the sample. If the relation between the conductivity of components and the effective conductivity is non-linear, the profile of the effective conductivity will be no longer exponential. In this case, a careful analysis accounting for the depth profile of the effective conductivity has to be carried out, e.g., the photoexcited layer can be approximated by a multilayered slab [25].

4. Overview of past experimental work

4.1. Organic semiconductors

The pioneering TRTS study on semiconducting polymers has been performed by Hendry et al. [26]. In a prototypic soluble polymer poly[2-methoxy,5-(2′-ethyl-hexyloxy)-*p*-phenylene-vinylene] (MEH-PPV), the authors found that photoexcitation first generates a certain density of separated electron–hole pairs, which recombine on the sub-picosecond time scale. Subsequently, the response is solely due to excitons. This dynamics was nicely resolved in the time-evolution of the THz conductivity spectra since separated electrons and holes have a response different from that of excitons. It was also confirmed that separated charges are stabilized upon adding an electron acceptor 1-(3-methoxycarbonyl)-propyl-1-phenyl-(6,6)C$_{61}$ (PCBM [27]) which captures electrons while the holes remain free to move along polymer chains. The studies were subsequently extended to characterize the role of inter-chain interactions. For high chain density in films, (hot) exciton dissociation yielding electrons and holes on different chains is possible and it results in a more efficient early-time charge generation compared to MEH-PPV solution with much lower chain density [28]. Unlike in MEH-PPV which exhibits charges with sub-picosecond lifetime, free charges generated in regioregular poly(3-hexylthiophene) (RR-P3HT) – which is characterized by a high long-range order – have a lifetime of several nanoseconds [29].

Much effort was devoted to the study of how various external parameters influence the transient THz conductivity spectrum and its ultrafast evolution. Particular attention was paid to the dependence on the excitation fluence [20,30,31]. In neat P3HT, the amplitude of the sub-picosecond conductivity peak scales almost linearly with the excitation fluence and this was attributed to the direct generation of separated charges. The fluence-independent decay rate then evidences that the initial recombination of separated charges is geminate. Conversely, the conductivity at long pump–probe delays depends sub-linearly on the excitation fluence which was attributed to non-geminate recombination of free charges. In P3HT:PCBM blends, both sub-picosecond and long-term transient conductivities scale almost linearly with the excitation fluence. Similar findings have been reported also for other polymers [31,32]. The role of PCBM concentration on the transient THz conductivity spectra is not as dramatic as in the case of bulk heterojunction power conversion efficiency. Though there is a certain optimum PCBM concentration which maximizes the transient conductivity, the transient conductivity does not drop to zero when PCBM is absent [20,33,34]. Variation of temperature and excitation wavelength has been also examined and it was found that, quite surprisingly, these parameters have almost no influence either on the dynamics or on the transient conductivity spectra [20,30,31,37].

Comparatively much less attention was devoted to exploit information encoded in transient conductivity spectra of separated charges. The spectra in all polymers for photovoltaics investigated so far exhibit a localized character, i.e., an increasing real part and negative imaginary part. The shape of the spectrum was modeled within a tight-binding approximation and the model accounted for the torsional disorder [35]. The results were successfully applied to PPV and P3HT polymers; on the other hand, a certain drawback that the amplitude of the calculated spectra has to be scaled to match the measured THz spectra [26,28,29,35]. In a few other works, the transient conductivity spectra were fitted by the Drude–Smith model [20,30,36]. The fits provide quite high values of the mobility and a very low quantum yield of free charges; these results are incompatible with the known internal quantum efficiencies of real operating solar cells based on nominally the same blends. It was demonstrated that there is a correlation between the amplitude of THz mobility and the mobility measured in field-effect transistor con-

figuration [32,33], but an explanation of the orders of magnitude difference between these mobilities is lacking. Transient conductivity spectra were also modeled as a sum of relaxation processes [34]. Later on, it was found that these two relaxation processes are related to the carrier localization on two different length scales and a model allowing the determination of the pertinent length scales was developed (Ref. [37] and Section 5).

The "localized" transport does not appear in all organic compounds. Notably, band-like transport described by a Drude model was reported in pentacene in the form of both single crystals and thin polycrystalline films [38–40]. Explanation of the paradox of low mobility incompatible with the band-like transport [41] was provided in terms of strong electron coupling to low-frequency phonon modes [42].

4.2. Semiconductor nanostructures

There have been many reports on measurements of transient conductivity in several semiconductor nanostructures based on various materials. The results have been interpreted using either the Drude, or the Drude–Smith model, in some cases combined with different effective medium approximations. However, a universal model or a more general explanation why quite different models have to be employed for different systems and structures is lacking.

The first TRTS experiments in semiconductor nanostructures have been carried out by the Schmuttenmaer group [7,19,25,43]. The measured transient conductivity spectra always exhibited a localized response. However, several different models were employed in order to explain the observed phenomena in different systems. Response of nanoparticle arrays of TiO$_2$ and InP was attributed to the disorder-limited transport and it was described in terms of the phenomenological Drude–Smith model [19,43]. For a suspension of CdSe nanoparticles, the Bruggeman effective medium approximation was combined with a Drude response of charges in individual nanoparticles to account for the observed shape of the spectrum [25]. An analogous approach was used to describe the THz conductivity of various ZnO nanostructures [7]. Here the Bruggeman effective medium approximation was used along with a description of the Drude–Smith response of individual charges.

THz conductivity is sensitive to the coupling between individual nano-components, as it was reported in arrays of InP and PbSe nanocrystals [43,44]. For example, it was found that the coupling strongly depends on the distance between the nano-components as well as on the material separating the nano-components.

The Drude–Smith model without further application of effective medium theories was used for the investigation of some other systems, including silicon nanocrystals [45,46] and InN nanorods [47]. In thin gold films, it was applied to characterize the degree of percolation of gold nanoparticles composing the films [48].

The importance of local field effects was demonstrated in the case of TiO$_2$ nanoparticles [24]. An effective medium approximation along with a Drude model succeeded in the explanation of transient conductivity of these TiO$_2$ nanoparticles as a function of both excitation fluence and temperature. The impact of local fields on the response of charges in isolated particles can be also understood in terms of oscillations of a charged plasma localized in the particles [21,49]. This explanation was also used for the interpretation of transient conductivity and its excitation fluence dependence in GaAs nanowires [50,51], or for the interpretation of spectral changes upon a metal insulator transition in VO$_2$, which occurs by a nucleation and growth of microscopic metallic domains [52].

It is interesting to note that some differences can be encountered between the spectra of steady state and photoexcited conductivity. A localized response was observed in the case of intrinsic electrons

in a porous InP structure, i.e., in a material where the semiconductor is percolated and its characteristic dimensions are larger than the electron mean free path [53,54]. On the other hand, the response in these structures became Drude-like for the photoexcited electrons. This counter-intuitive behavior was attributed to the surface depletion layer, which effectively reduces the area for free electron motion in the ground state, while in the photoexcited state this layer may be significantly reduced.

In this paper we focus on the response of free electrons in nanostructures. However, in some specific cases other excitations may contribute as well. In the steady state, response of lattice vibrations may be important [55]. In photoexcited systems, excitons may exist and their conductivity at THz frequencies is then proportional to $-if$ [56,57].

5. Microscopic models of the far-infrared response

5.1. Hopping along polymer chains

An illustrative model of the response of charge carriers on polymer chains was developed by Prins et al. The model assumes that charge transport on polymer chains is purely diffusive (characterized by a diffusion coefficient D) and the charge confinement is only due to reflecting (infinite) barriers enclosing the polymer chain length L. The mobility spectrum is then described by the series [58,59]

$$\mu(\omega) = \frac{8eD}{k_B T} \cdot \sum_{k=0}^{\infty} \frac{C_k^{-2}}{1 - C_k^2 D/(i\omega L^2)} = 8\mu_{int} \cdot \sum_{k=0}^{\infty} \frac{1}{C_k^2} \frac{i\omega\theta_k}{i\omega\theta_k - 1}, \quad (15)$$

where k_B is the Boltzmann constant, $\mu_{int} = eD/(k_B T)$ is the intrachain mobility, and $C_k = 2\pi(k + 1/2)$. The right-hand expression of Eq. (15) shows that this formula is a sum of Debye-like relaxations [Eq. (7)] with relaxation times $\theta_k = L^2/(C_k^2 D)$. For $\omega \to \infty$, the series can be summed: the result approaches μ_{int} and the summand with $k = 0$ clearly dominates. A natural approximation of Eq. (15) is thus a single Debye-like relaxation [37]

$$\mu(\omega) \approx \mu_{int} \frac{i\omega\theta_0}{i\omega\theta_0 - 1} \quad (16)$$

with relaxation time

$$\theta_0 = \frac{eL^2}{\pi\mu_{int}k_B T}. \quad (17)$$

This expression links the length scale (L) and a characteristic frequency [$1/(2\pi\theta_0)$] above which the barriers do not influence the mobility spectrum. For illustration, a chain with a length $L = 10$ nm and an intrachain mobility $\mu_{int} = 10$ cm^2 V^{-1} s^{-1} yields $\theta_0 = 1.2$ ps and $1/(2\pi\theta_0) = 0.13$ THz. Dispersion in the THz range will be thus observed only for short distances between the barriers and high intrachain mobility. The relaxation time increases rapidly with the barrier distance and for chain lengths of a typical polymer the relaxation shifts to the microwave region, in which case the effects related to a finite polymer chain length can be neglected in the THz spectral region.

Calculation of the mobility spectra in a more general situation, such as for charges on polymer chains containing partially reflecting barriers (representing breaks in conjugation along the polymer chain) or traps, can be efficiently accomplished by a Monte-Carlo method [37]. In this method, a series of simulations is performed to find (stochastic) trajectories of charge carriers. These trajectories are controlled by the probability of hopping from one repeat unit to another. Specific forms of these probabilities allow one to model the influence of barriers or traps on the charge motion. The mobility spectrum $\mu(f)$ is then calculated from the autocorrelation function of carrier position using the Kubo formula [60].

For simplicity, we consider straight polymer chains containing equidistantly spaced repeat units with length a. The chain is terminated by perfectly reflecting (infinite) potential barriers enclosing N repeat units. The carriers can hop between the nearest neighboring unit and the mean time for the hop to a given neighbor is τ_{hop}. In this situation, the diffusion coefficient D_{int} describing the carrier motion on an infinite chain without defects equals a^2/τ_{hop}, and the Einstein's relation then provides the intrachain mobility (mobility of charges moving on an infinite chains without defects):

$$\mu_{int} = \frac{ea^2}{k_B T\tau_{hop}}. \quad (18)$$

Firstly, we investigate the influence of potential barriers enclosing segments of N_β repeat units (Fig. 4a). The mean time for passing over the barrier is denoted τ_β. Infinite barriers are characterized by $\tau_\beta \to \infty$, while absence of barriers is equivalent to setting $\tau_\beta = \tau_{hop}$. In Fig. 4b, the mobility spectra are plotted for carriers moving along the chains containing infinite and finite potential barriers. When the barriers are infinite ($\tau_\beta \to \infty$), the spectrum can be accounted for by a single relaxation term, in agreement with Eq. (16). Its relaxation time θ_a is short for short segment lengths and it increases with N_β. Substituting Eq. (18) and $L = aN_\beta$ into Eq. (17) we get

$$\theta_a = \tau_{hop} \cdot \left(\frac{N_\beta}{\pi}\right)^2, \quad (19)$$

which is confirmed by the simulations (Fig. 4c). Lowering the barriers (i.e., using a finite τ_β) results in a growth of the low-frequency mobility and an additional relaxation with a longer relaxation time θ_b is then required to fit the calculated spectra. The short and long relaxation times correspond to the diffusion times along the segments and along the entire chain, respectively. More generally, introduction of a localization process on a specific length scale gives rise to an additional relaxation with a relaxation time expressing the diffusion time on the appropriate length scale. Since N_β in Eq. (19) must be greater or equal to two, it turns out that θ_a cannot be shorter than $\tau_{hop} \cdot (2/\pi)^2$. In other words, the value of θ_a (which can be found e.g. by fitting experimental data) imposes the upper limit on the value of the hopping time τ_{hop}.

Secondly, we study the response of chains containing potential wells (traps) located regularly at each N_ωth repeat unit (Fig. 5a). In this case, the mean release time is $\tau_\omega/2$ and absence of traps is represented by the value of $\tau_\omega = \tau_{hop}$. A typical mobility spectrum of carriers on a polymer chain with potential wells is shown in Fig. 5b. Regardless of the density of traps and of the release time τ_ω, the spectra are always described essentially by a *single* relaxation term. Increasing the density of potential wells N/N_ω results in a decrease of the mobility nearly without the change of its spectral shape (i.e., there is only a slight change of the relaxation time θ_a). For low trap densities, we can thus formally consider that a part of carriers moves along the chains without traps and their fraction is reflected in the quantum yield ξ. The remaining carriers are trapped in states not contributing to the THz conductivity. Even with the known fraction of trapped carriers $(1 - \xi)$, it is not possible to determine unambiguously the density of traps N/N_ω and the release time τ_ω since increasing N_ω has almost the same effect as decreasing τ_ω.

The mobility spectra in Fig. 4b can be formally fitted by the Drude–Smith model [Eq. (9)]. However, in this case, the parameters of the Drude–Smith expression have no physical meaning; at the best, it is possible to find some formal relation between the parameters τ_s and c_1 of the Drude–Smith model and the microscopic quantities such as τ_{hop} and τ_β/τ_{hop} employed in the simulations.

When comparing the mobilities calculated within the framework described above, it is important to recall that we calculated the mobility of carrier motion in one dimension. In experiment,
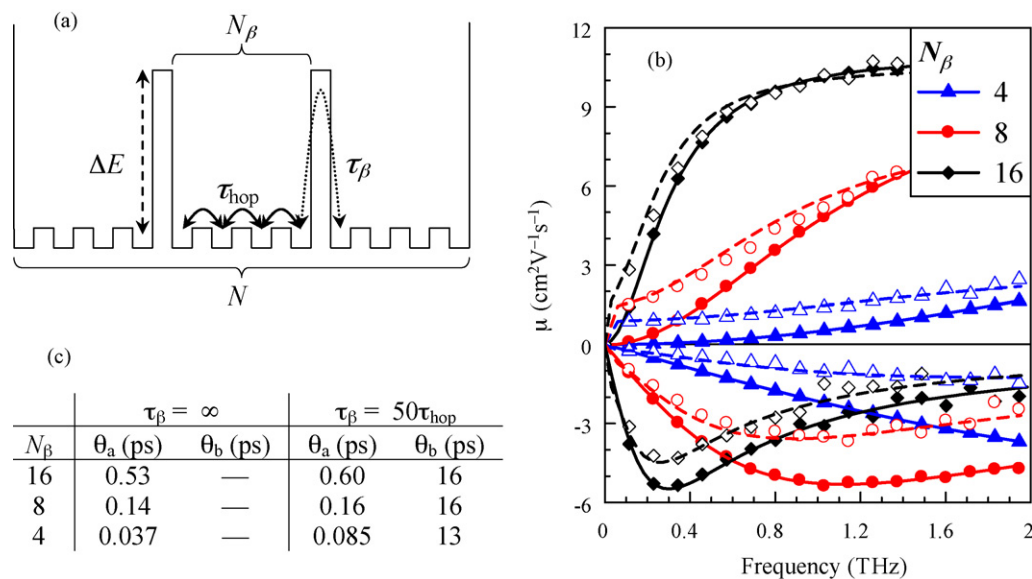
Fig. 4. (a) Scheme of the potential profile and corresponding mean transition times for the simulation of mobility on polymer chain with partially reflecting barriers. (b) Calculated mobility spectra of charges moving on polymer chains with infinite ($\tau_\beta = \infty$, closed symbols) and finite ($\tau_\beta = 50\tau_{hop}$, open symbols) barriers and for several numbers N_β of repeat units enclosed between the barriers (the total polymer chain length was $N = 32$). Solid lines: fits of spectra calculated for the infinite barriers by a single relaxation term; dashed lines: fits of spectra calculated for the finite barriers by two relaxation terms. (c) Parameters of the fits from (b). The hopping time was $\tau_{hop} = 22$ fs [after Ref. [37]].

mostly solutions or thin films consisting of *randomly* oriented polymer chains are investigated. The calculated mobilities must be thus multiplied by the factor of 1/3 to account for the random orientations of polymer chains.

A similar approach considering either the barriers or the traps has been employed in Ref. [61] for the calculation of time dependence of the diffusion coefficient and mobility along polymer chains containing a Gaussian distribution of energies of barrier heights or trap depths. Here we concentrate on the calculations of the mobility spectra at THz frequencies. We set the height of the barriers or the depth of the traps to one given value; this approach clearly illustrates the influence of such defects on the THz mobility spectra. Within the developed theoretical framework, it is straightforward to consider a realistic distribution of barrier heights or trap depths

which would be closer to the situation in a real polymer and more adequate for comparison with experimental data.

5.2. Band-like transport in nanoparticles

The microscopic picture of band-like transport in non-degenerate semiconductors is in fact a Brownian motion of charge carriers. Most of the time, the carriers move freely and only occasionally, they scatter e.g. due to an interaction with phonons. Inside semiconductor nanoparticles with sizes much larger than the charge carrier Bohr radius, it is reasonable to assume that the motion is the same as in the bulk material described by the mean scattering time τ_s. In the model, each scattering event results in a randomization of the velocity vector v according to
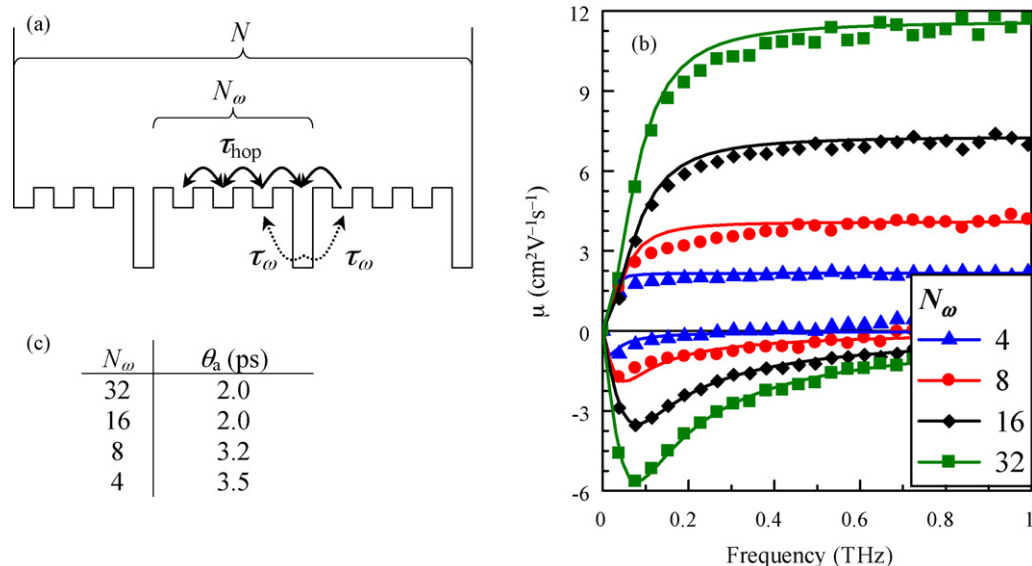
Fig. 5. (a) Scheme of the potential profile and corresponding mean transition times for the simulation of mobility on polymer chain containing trap sites. (b) Calculated mobility spectra of charges moving on polymer chains with traps characterized by the mean release time $\tau_\omega = 20\tau_{hop}$ (symbols). The total polymer chain length was $N = 32$. Lines: fits of spectra by a single relaxation term. (c) Parameters of the fits from (b). The hopping time was $\tau_{hop} = 22$ fs [after Ref. [37]].
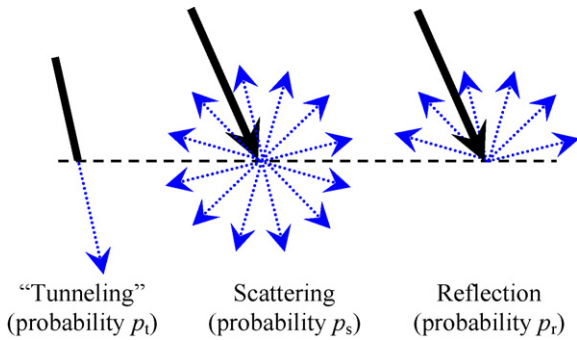
Fig. 6. Scheme of processes which can occur in a nanoparticle upon carrier interaction with the nanoparticle surface (dashed line). Thick line represents the incident carrier; the dotted arrows indicate possible trajectories after photoexcitation. Upon scattering event, the charge carrier can travel any direction. Upon reflection event, the charge carrier remains in the original nanoparticle.

the Maxwell–Boltzmann distribution, which allows accounting for the carrier temperature. Unlike in bulk, carriers in semiconductor nanostructures can interact with the surface which can be described in terms of the following three probabilities ($p_t + p_s + p_r = 1$; Fig. 6):

- With a probability p_t the carrier continues its motion without interacting with the nanoparticle boundary.
- The nanoparticle boundary isotropically scatters the carrier with probability p_s which means that there are equal probabilities that the carrier enters another nanoparticle or that the carrier remains in the original one.
- The carrier is reflected (scattered) back to the original nanoparticle with a probability p_r. Such a process arises due to energy barriers between the nanoparticles and it is the only process leading to the carrier localization.

The probability that the carrier remains in the original nanoparticle (it is scattered back) is thus $p_b = p_r + p_s/2$ while the probability that it enters another one is $p_f = p_t + p_s/2$ and this probability can be understood as a permeability of the nanoparticle boundary.

A Monte-Carlo method is used to simulate trajectories representing the stochastic motion of charge carriers. The mobility of carriers is then calculated using the Kubo formula [62]

$$\mu_{ij}(\omega) = \frac{e}{k_B T} \int_0^\infty \left[\langle v_i(0)v_j(t) \rangle \exp(i\omega t) \mathrm{d}t \right], \tag{20}$$

where the averaging <...> takes place over a canonical ensemble of carriers represented by a temperature T. It is possible to perform the simulation in almost any geometry. For the sake of simplicity, we mostly consider spherical or cubical nanoparticles. Such systems are macroscopically isotropic, therefore the mobility tensor is diagonal and the diagonal elements of the mobility tensor μ_{ii} are equal to each other.

It turns out that the shape of the spectrum is determined only by the parameters p_t, p_r, p_s and $\alpha = d/l_{free}$ (d is the nanoparticle size and $l_{free} = v_{therm}/\tau_s$ is the carrier mean free path where $v_{therm} = \sqrt{3k_B T/m}$ is the thermal velocity). The remaining parameters (τ_s, d, T) only determine the pertinent scales of length, time, frequency and mobility amplitude. By analysis of Eq. (20), one can find specific scaling rules which are important for subsequent discussion and for the reduction of the number of representative simulations [11] (in the following we do not consider the carrier mass m as a variable parameter).

Examples of the calculated complex mobility spectra for isolated nanospheres ($p_r = 1$) are shown in Fig. 7. The mobility approaches zero at sufficiently low frequencies for finite α since the local-
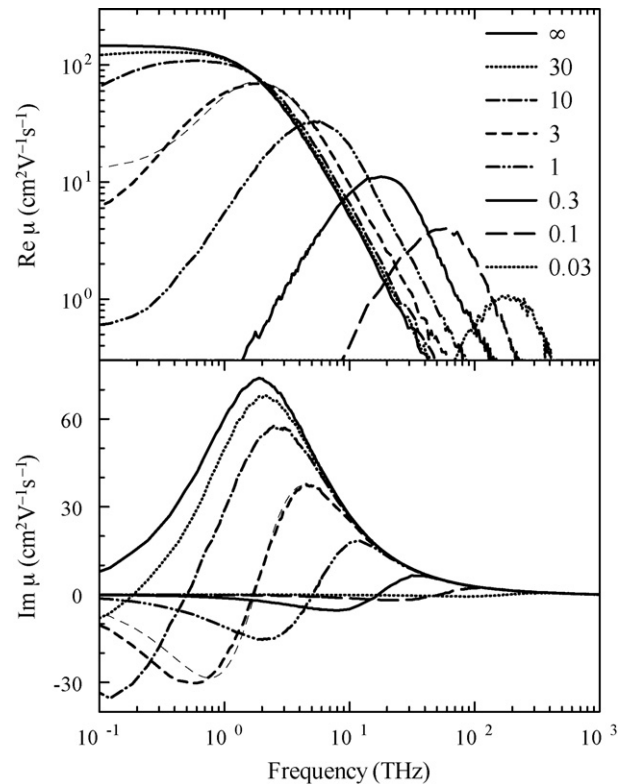
Fig. 7. Mobility spectra of charges in nanospheres calculated using the Monte-Carlo method for $p_r = 1$ and $p_s = p_t = 0$ for various values of α. The other parameters of the simulation were $l_{free} = 10$ nm, $v_{therm} = 1.17 \times 10^5$ m s^{-1} ($T = 300$ K) and $\tau_s = 85.6$ fs. The thin dashed line illustrates a Drude–Smith fit over the entire plotted spectral range for $\alpha = 3$ which yields parameters $\tau_{DS} = 83$ fs and $c_1 = -0.912$ (the line is not shown above 5 THz as it is indistinguishable from the line corresponding to the mobility calculated by the Monte-Carlo method) [after Ref. [11]].

ization cancels the long-range transport. The real part of the mobility spectrum shows a peak, therefore the imaginary part must become negative in a certain spectral interval in order to satisfy the Kramers–Kronig relations (analogously to the conductivity spectrum of bound charges [8]). The peak in the real part decreases in amplitude and its frequency f_0 shifts to higher frequencies upon decreasing α (enhanced localization). The position of the peak is closely related to the ballistic round-trip time of carriers $\tau_{rt} = 2d/v_{therm}$: we find that a relation $f_0 \approx 0.9/\tau_{rt}$ is quite well satisfied in spherical nanoparticles for $\alpha \lesssim 30$. With increasing α more scattering events occur during the round trip and for $\alpha \gtrsim 30$ the resonance frequency is no longer well defined in the spectra. The decrease of the conductivity amplitude with decreasing α is related to the fact that the effective carrier scattering is enhanced by frequent reflections at the nanoparticle surface.

The spectrum then approaches the Drude model as the probability p_r decreases to zero (Fig. 8). The most remarkable difference consists in a non-vanishing real part of the mobility at zero frequency, which is caused by the fact that the charges may pass from one nanoparticle to another and the long-distance transport is thus enabled. Other features (peak in the real part of the mobility shifting with α, negative imaginary part of the mobility at low frequencies) are similar to the preceding case. For $p_r = 0$ the carrier localization is lost and the nanoparticle boundaries contribute merely to the isotropic scattering process ($p_s = 1$) or they have no influence ($p_t = 1$). The mobility is then described by the Drude formula; in the former case, the effective carrier scattering time is shortened compared to the bulk material. Such a type of behavior was observed in CdSe nanoparticles [25].
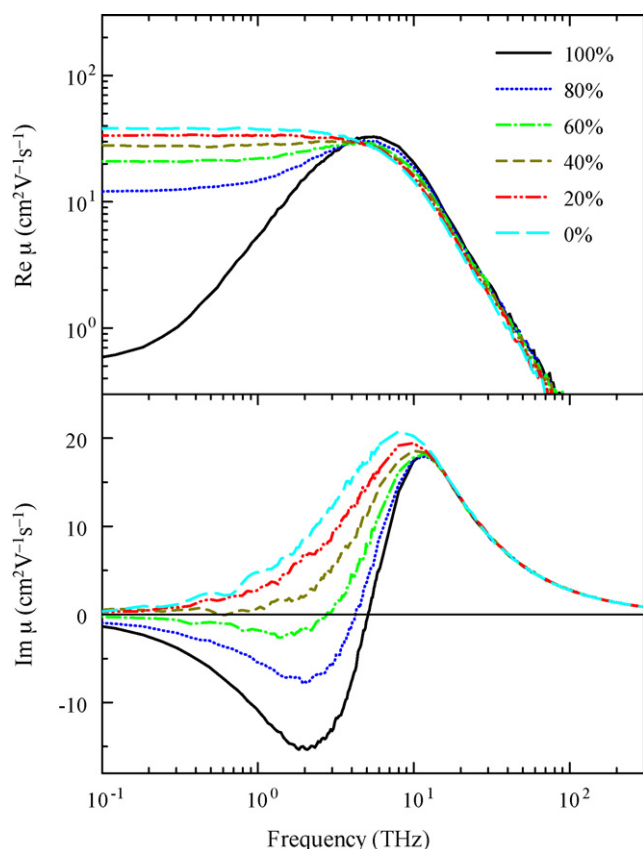
Fig. 8. Mobility spectra of 10-nm semiconductor nanoparticles calculated using the Monte-Carlo method for various p_r. The other parameters of the simulation were $l_{\text{free}} = 10\,\text{nm}$, $v_{\text{therm}} = 1.17 \times 10^5\,\text{m\,s}^{-1}$ ($T = 300\,\text{K}$), $\tau_s = 85.6\,\text{fs}$, $p_t = 0$ and $p_s = 1 - p_r$.

It should be noted that the entire conductivity spectra calculated using the Monte-Carlo method cannot be fitted by the Drude–Smith model. However, it is interesting to note that when a restricted spectral region (spanning over about a decade in frequencies or less) is considered, the spectrum can be reasonably well approximated by Eq. (9).

The simulations can be straightforwardly extended to describe the response of more complex systems, including either complex shapes or systems with more than one conducting component. For example, transient THz conductivity was investigated in nanocrystalline mesoporous films grown by "bricks and mortar" technology [63,64]. This material is characterized by a high crystallinity and simultaneously it is porous which is achievable at low calcination temperature. The properties are controlled by preparation conditions, namely by the proportion between the crystalline "bricks" and the amorphous "mortar". Subsequent calcination leads to the seeded growth of the nascent crystallites. Simulations of the THz mobility spectra of photogenerated electrons made it possible to find a mean size of the crystallites and to show that a connectivity between the crystallites (which are rather distant from each other) exists.

Temperature-dependent studies constitute a powerful test of transport mechanisms in bulk semiconductors. Due to the substantial dependence of the mean free path on temperature, the model developed above predicts a strong dependence of the mobility spectra on temperature in nanostructures (Fig. 9). The temperature dependence of the transient THz conductivity was studied experimentally in detail in microcrystalline silicon [65]. This material exhibits a complex structure, consisting of large grains surrounded by an amorphous tissue. The large grains with size of hundreds of nm are built of small grains with typical size of about 20 nm
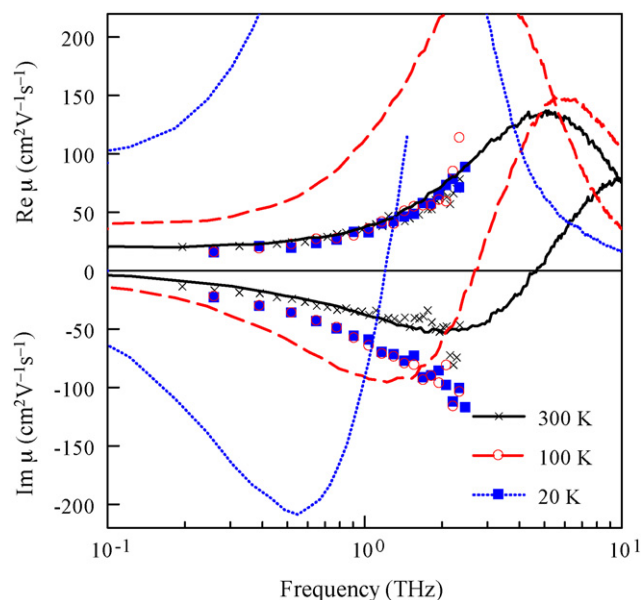

Fig. 9. Symbols: mobility spectra of microcrystalline silicon (58%-crystallinity) measured 50 ps after photoexcitation at 800 nm and at various temperatures. Lines: results of Monte-Carlo calculations of mobility in 20-nm silicon grains with grain-boundary reflectivity $p_r = 0.98$ for various temperatures [after Ref. [65]].

[66]. Fig. 9 shows the conductivity spectra measured at 50 ps after photoexcitation when the charge carriers should be in thermal equilibrium with the lattice. At room temperature, it was possible to describe the response by using our model of band-like transport of charge carriers confined within the small grains. However, in contrast with the Monte-Carlo simulations, the experimental conductivity spectra show very weak temperature dependence (Fig. 9). These discrepancies at low temperatures between the simulations and the experimental spectra lead to a rejection of the interpretation based on an intra-grain band-like transport of carriers. The observed response was instead assigned to hopping between surface states on the small grain boundaries [65].

6. Ultrafast dynamics in polymer:fullerene blends

We investigated in detail the ultrafast dynamics in a blend of a low-band-gap polyphenylene LBPP-1 and PCBM and in a blend of a low-band-gap polyfluorene APFO-3 and PCBM. The polyphenylene LBPP-1 consists of an alternating sequence of two types of monomer units: a low-band-gap segment and a dialkoxy-phenylene unit [67]. The polymer APFO-3 (poly[2,7-(9,9-dioctyl-fluorene)-alt-5,5-(4′,7′-di-2-thienyl-2′,1′,3-benzo-thiadiazole)]) also consists of two different types of monomer units: a fluorene unit, and a low-band-gap segment of benzo-thiadiazole [68]. Both copolymers have a rather low-band gap: the absorption of APFO-3 extends up to 650 nm and LBPP-1 exhibits an additional near-infrared absorption band extending to more than 1100 nm. This makes them interesting for photovoltaic applications since they can harvest a significant fraction of the solar spectrum.

The individual copolymers were dissolved in chloroform and blended with the soluble fullerene derivative PCBM. Approximately 1 μm thick films were prepared by drop-casting the solution on fused silica substrates. The transient THz conductivity was measured in usual setups for optical pump–THz probe experiments [65]. The density of excitations was about $8 \times 10^{19}\,\text{cm}^{-3}$. This is many orders of magnitude more compared to the standard solar intensity and it is also near the threshold where the non-geminate recombination starts to be effective in APFO-3:PCBM blend [69]. Since the dynamics in APFO-3:PCBM has been shown to be exci-
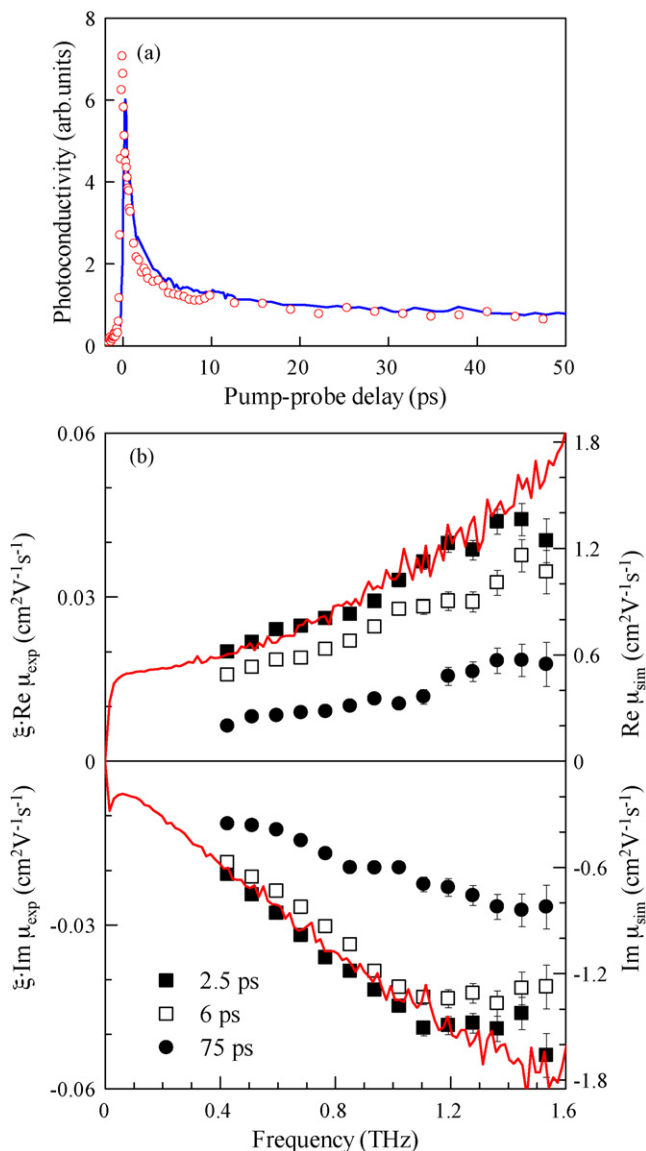
Fig. 10. (a) Pump–probe scan measured in the LBPP-1:PCBM blend (1:4) upon excitation at 620 nm (line) and 800 nm (symbols). (b) Measured spectrum of transient conductivity in the LBPP-1:PCBM blend at three representative pump–probe delays upon photoexcitation at 620 nm (symbols, left axis) and mobility obtained in the Monte-Carlo calculations (lines, right axis) [after Ref. [37]].

tation independent below this threshold [69], we believe that our observations are relevant for the solar illumination regime as well.

6.1. Experimental results

A pump–probe scan without spectral resolution, expressing the time dependence of the average THz photoconductivity of the LBPP-1:PCBM blend, is shown in Fig. 10a. It displays an instantaneous activation followed by a sub-ps decay. The decay then slows down so that a non-vanishing signal is observed even 1 ns after photoexcitation. Examples of measured transient conductivity spectra for a few pump–probe delay times are shown in Fig. 10b for the LBPP-1:PCBM blend. Their shape does not change significantly with τ_p which indicates that the transport mechanism does not change, and that only density of mobile carriers decays.

The transient conductivity can in principle originate both from positive and negative charges. Following photoexcitation, the electron is rapidly transferred to the fullerene ball and the hole remains

on the polymer chain [70,71]. We found experimentally that direct above-gap excitation (400 nm) of PCBM produces a signal with comparable magnitude and with a very short lifetime (~0.5 ps). However, the long wavelengths employed for the photoexcitation of blends are absorbed mainly in the polymer and not in the PCBM, hence the signal from direct excitation of PCBM is only marginal. This implies that the observed conduction is mainly due to holes moving along polymer chains. This view is also supported by the Stark spectroscopy which showed that the electron mobility in PCBM at early time is only 0.0048 cm^2 V^{-1} s^{-1} [13].

Based on the results presented in Section 5.1 (model in Fig. 4), we conclude that the shape of the conductivity spectrum represents charge hopping along polymer chains containing closely spaced potential barriers of finite height. In the Monte-Carlo simulations of the mobility spectra of the LBPP-1:PCBM blend we considered τ_{hop} equal to 22 fs which corresponds to the time a hole needs to traverse the repeat unit length at thermal velocity. In fact, the rapid increase in the real part of conductivity excludes the possibility that the hopping time is longer than this value [cf. Eq. (19) and discussion below]. This means that the intrachain mobility is rather high: 40 cm^2 V^{-1} s^{-1} [Eq. (18)]. The shape of the observed conductivity spectrum for pump–probe delays ≥2.5 ps is then best matched with parameters $N_\beta = 4$, $\tau_\beta = 1.9$ ps, and $N \gtrsim 26$. The presence of *finite* potential barriers (finite τ_β) and the distant chain terminations (large N, consistent with the number average of repeat units per chain x_n of LBPP-1 [67]) appear in the spectra as the non-vanishing real part of conductivity at the lowest THz frequencies. The small value of N_β is then related to the rapid increase of the conductivity with frequency.

Very similar behavior was observed in the APFO-3:PCBM blends [34]. In Fig. 11 we illustrate the comparison between the measured data and mobility spectrum calculated by the Monte-Carlo method. The repeat unit length is now ~2.1 nm. Assuming that holes move at thermal velocity yields $\tau_{hop} = 31$ fs and intrachain mobility $\mu_{int} = 55$ cm^2 V^{-1} s^{-1}. The shape of the observed conductivity spectrum is then best matched with parameters $N_\beta = 4$, $\tau_\beta = 1.1$ ps and $N \gtrsim 8$ which are quite close as those found for the LBPP-1:PCBM blend.

In both blends, there is a large difference between the calculated mobilities and the measured yield-mobility products (Figs. 10 and 11) which shows that only a minority of initially generated charges remains mobile a few ps after photoexcitation. We can estimate the yield as the ratio between the measured yield-mobility product and the calculated mobility. For example, 2.5 ps after photoexcitation the yields are 3.2% in APFO-3:PCBM and 1.6% in LBPP-1:PCBM and they further decrease with increasing pump–probe delay. These yields are much smaller than the internal quantum efficiency which represents the yield of charge carriers at very long time scales and which in both investigated blends substantially exceeds 10% [67,68]. This leads us to the conclusion that most of the photoexcited charges are trapped on the picosecond time scale, i.e., they do not contribute to the THz spectra but they can still mediate slow conduction on long time scales [3].

In Ref. [37] we also studied in detail the sub-picosecond dynamics in the LBPP-1:PCBM blends. Since it is faster than the probing THz pulse length, special methods based on a two-dimensional Fourier transformation [72,73] were applied for the transient conductivity retrieval. We found that the conductivity spectra at sub-ps time scale are qualitatively similar as those presented in Fig. 10b. It is possible to match them with the same value of N_β, but with a shorter time for hopping over barriers: $\tau'_\beta = 0.3$ ps. The hopping over the barriers is thus easier at short times and less efficient at longer times. This can be understood as a result of carrier cooling when the initial excess energy facilitates hopping over barriers. We also identified two decay times – 180 fs and 860 fs – which correspond to the cooling and trapping times, respectively.
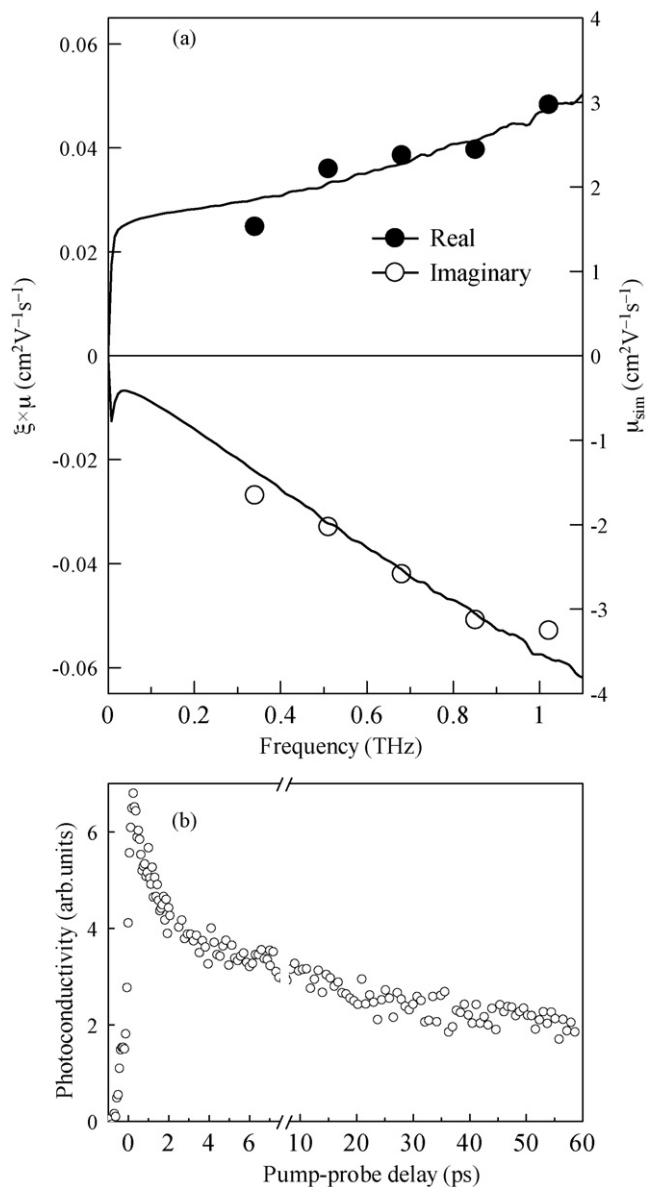
Fig. 11. (a) Measured transient conductivity spectrum in the APFO-3:PCBM blend at the pump–probe delay of 2.5 ps along with the result of Monte-Carlo simulation. (b) Kinetics in the APFO-3:PCBM blend. These data were measured with the excitation fluence of 3×10^{14} ph/cm^2 and with the excitation wavelength of 580 nm.

6.2. Resulting picture

A detailed analysis of visible transient absorption measurements carried out on APFO-3:PCBM blends has been performed in Ref. [69]. This study was recently extended to two other acceptors, C$_{70}$-PCBM and C$_{70}$-BTPF [74], with the same APFO-3 polymer and the results provide information about charge generation, separation and recombination in BHJ films. Charge separation and formation of mobile charges contributing to the photocurrent is a key process of a functioning solar cell, which is poorly understood. By combining the results from the visible and THz transient absorption measurements we can shed some light on how this happens [74]. Photoexcitation of the polymer results in generation of a bound polaron pair with a characteristic formation time of 100–200 fs, somewhat dependent on the driving force for charge transfer. This charge pair further separates under the influence of the very high early-time charge mobility observed in the THz experiments. In a BHJ film with no internal electric

field, the charges only separate a few nanometers, how much depends on the properties of the BHJ material, and then recombine on the nanosecond to hundreds of nanosecond time scale. In a functioning solar cell with an internal electric field, the somewhat separated, but still interacting, charges are fully separated into free mobile charges that can be extracted from the material and contribute to the photocurrent. Decreased Coulomb attraction as a result of medium polarization, polaron formation and its dynamic nature resulting in time fluctuating screening, probably are important features in the free charge formation process [74].

7. Dynamics and transport in bare and sensitized semiconductor nanoparticles

The operation of a dye-sensitized solar cell relies on the efficient electron injection from a photoexcited sensitizer molecule to the conduction band of a semiconductor (often wide band-gap metal oxides) [75,76]. The product of this process is a mobile electron and an oxidized sensitizer (cation). The generally accepted picture is that mobile electrons appear in concert with injection. Our results show that charge injection and formation of mobile charges are not necessarily directly connected, and that charge transport in the active solar cell material can be different from that in non-sensitized semiconductors. This is related to strong electrostatic interaction between injected electrons and dye cations at the surface of the semiconductor nanoparticle.

We take advantage of combining results of visible and THz pump–probe spectroscopy. Probing in the visible and infrared range typically provides information about the electronic state of the dye molecules, i.e., the formation of oxidized dye molecules (cations) upon electron injection [75,77–80] is monitored. Probing in the THz spectral range is sensitive to the transport of mobile charge carriers (injected electrons). Several reports on measurement of transient THz conductivity in bare and sensitized TiO$_2$ and ZnO nanoparticles were previously published [7,19,24,81,82], but they did not establish a comprehensive picture of the ultrafast charge transport.

We investigated in detail [83] the dynamics in ZnO and TiO$_2$ nanoparticle thin films (mean particle diameters 15 and 9 nm, respectively) sensitized by Zn(II)-5-(3,5-dicarboxyphenyl) phenyl-10,15,20-triphenylporphyrin (ZnTPP-Ipa) [84] and Ru(2,2′-bipyridyl-4,4′-dicarboxylic acid)$_2$(NCS)$_2$·2H$_2$O (Ru-N3) dyes [85]. The transient THz conductivity was measured in usual setups for optical pump–THz probe experiments [65]. Two different states were induced by different excitation wavelengths: either electron–hole pairs were generated in the semiconductor nanoparticles by above-gap pumping (266 nm or 300 nm), or the dye molecules were excited by radiation in the absorption band of the respective dyes (558 nm for ZnTPP-Ipa, 400 nm for Ru-N3). Transient absorption (TA) experiments were performed using a standard TA spectrometer based on a 1 kHz laser amplifier [86]. The pump pulse was polarized at the magic angle to the polarization of the white-light-continuum probe.

7.1. Ultrafast dynamics

In Fig. 12a we see that after the excitation of the dye in sensitized ZnO, the rise of the photoconductivity which represents the population of injected mobile electrons (e$_{mobile}$) occurs on the tens to hundreds-ps time scale. The corresponding rise for dye-sensitized TiO$_2$ occurs on the sub-ps and few ps time scale (Fig. 12a). The fact that ZnO films sensitized by both dyes behave in the same way shows that the slow injection of mobile electrons is related to a property of ZnO nanoparticles rather than to a particular dye
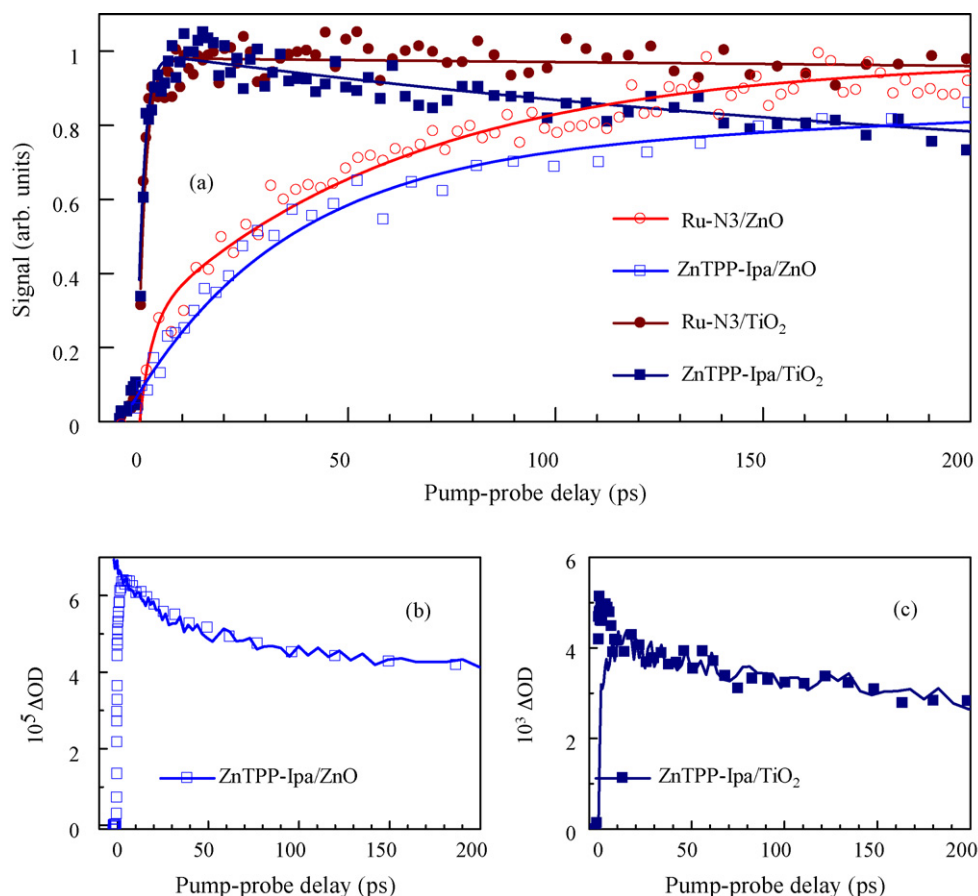
Fig. 12. (a) Evolution of transient THz conductivity (normalized to unity). The lines serve only to guide the eye. (b) Transient absorption of ZnTPP-Ipa/ZnO probed at 655 nm (symbols). This wavelength was selected due to the largest difference between the transient absorption of the initially excited state D* and of the excitation products. The line represents a vertically flipped and shifted transient THz conductivity of ZnTPP-Ipa/ZnO from (a). (c) Transient absorption of ZnTPP-Ipa/TiO$_2$ probed at 655 nm (symbols). The line represents a shifted and scaled transient THz conductivity of ZnTPP-Ipa/TiO$_2$ from (a) [note that the line is not flipped, unlike in panel (b)] [after Ref. [83]].

molecule. Mid-IR probe of injection of conduction band electrons in Ru-N3/ZnO has previously demonstrated a similar slow kinetics [77,87] which means that both THz and mid-IR radiation probe mobile electrons.

Combination of results by time-resolved THz and TA spectroscopy makes it possible to gain detailed new knowledge on the injection and recombination mechanisms. The TA spectra and kinetics measured in the interval 560–740 nm were fitted globally which revealed that the spectra can be decomposed into three species associated spectra corresponding to the initially excited state D*, the resulting dye cation D$^+$ and an intermediate state (Fig. 13). The shape of the cation spectrum is very similar to those previously reported [88,89] and clearly distinct from other long-lived potential photoproducts, e.g. triplets [90,91]. The intermediate state is formed within ~5 ps. The rate of its decay is the same as the rate of the THz signal rise (attributed to the formation of mobile charges, Fig. 12b) and its spectrum resembles that of D$^+$. In the experiments of Katoh et al. on Ru-N3/ZnO [92] a species with spectral characteristics similar to that of the Ru-N3 cation (termed exciplex) was observed immediately after excitation (~100 fs). Thus, for ZnO sensitized with both ZnTPP-Ipa and Ru-N3 the formation of a species with spectral properties similar to those of the oxidized dye is very fast (<5 ps) and precedes the cation formation.

The THz and TA results for dye-sensitized ZnO can together be understood within the kinetic scheme of Fig. 14a. Photoexcitation of the sensitizer (1) leads to an electron–cation (EC) complex within ~5 ps (3) in which the electron is strongly bound to the cation and therefore it does not contribute to the THz signal, whereas the TA

spectrum of the EC complex is similar to that of the cation (Fig. 13). This bound EC state can either recombine (5) or dissociate into a mobile electron in ZnO and cation (4). The initial part of the TA decay of ZnTPP-Ipa/ZnO (Fig. 12b) reflects the depopulation of the EC complex caused by recombination (5) (approx. 75%) and cation
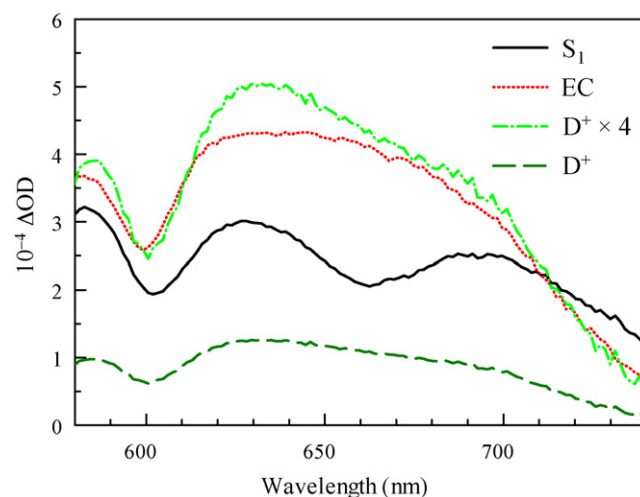
Fig. 13. Species associated spectra obtained from a global fit of the transient absorption spectra measured in ZnTPP-Ipa/ZnO. Shown are spectra of the initially excited state (S1), electron–cation complex (EC) and of the ZnTPP-Ipa cation (D$^+$). D$^+ \times 4$ denotes the spectrum D$^+$ multiplied by 4.
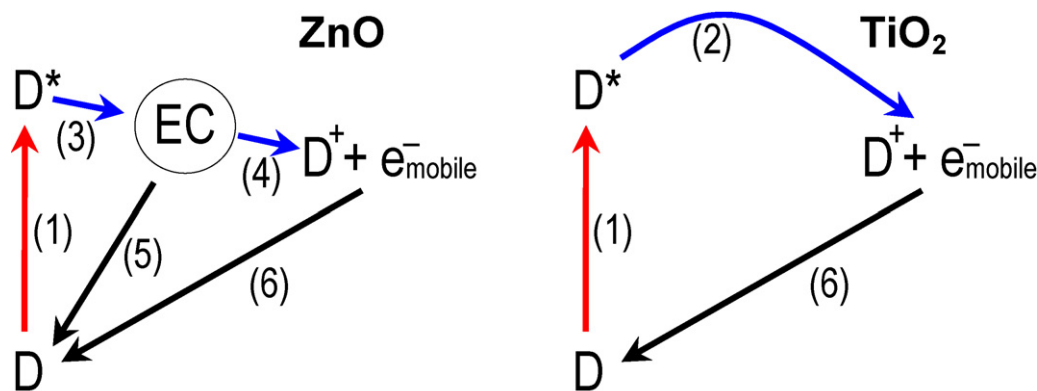
Fig. 14. Scheme of the processes in dye-sensitized ZnO and TiO$_2$. (1) Dye excitation, (2) direct electron injection, (3) formation of an electron–cation (EC) complex, (4) dissociation of EC complex, (5) recombination of EC complex and (6) charge recombination. D – dye molecule [after Ref. [83]].

formation (4) (approx. 25%). Because of the very slow recombination of injected electrons (6), the THz signal at long times ($\gtrsim$1 ns) reflects the total population of injected mobile electrons, which is equal to the population of cations. From the scheme in Fig. 14 it can be predicted that the measured formation rate of mobile electrons should be equal to the observed decay rate of the EC complex through pathways (4) and (5). This is indeed confirmed by the perfect match of the rise of the THz kinetics and the decay of TA kinetics (see Fig. 12b where the two kinetics are superimposed). Since there is no significant THz signal immediately after photoexcitation, we conclude that there is no substantial amount of mobile electrons injected into ZnO directly. Note that the recombination (5) of the EC complex limits the number of mobile electrons injected into the conduction band of the semiconductor. We thus conclude that the EC complex recombination may decrease the efficiency of ZnO-based solar cells.

The injection/recombination dynamics observed for sensitized nanocrystalline TiO$_2$ films is fundamentally different from that observed for sensitized ZnO. The THz and TA kinetics of both dyes (Fig. 12a and c and Refs. [75,77–80,87]) show that both cations and mobile conduction band electrons appear on the same ultrafast time scale (100 fs–10 ps). This suggests that charge injection into TiO$_2$ is a direct process [(2) in Fig. 14]. Slow electron–cation recombination (6) occurring on a hundreds-ps time scale and longer is observed in ZnTPP-Ipa/TiO$_2$ as the decays in the TA and THz signals (Fig. 12a and c). The common origin of these processes is underlined by the same decay rates, as shown in Fig. 12c. The THz conductivity for Ru-N3/TiO$_2$ does not start to decay even on the nanosecond scale whereas it decays with ∼1 ns lifetime in ZnTPP-Ipa/TiO$_2$ which may negatively influence the efficiency in real solar cells.

7.2. Transient THz conductivity

Transient far-infrared conductivity spectra (Fig. 15) provide information on the local transport of carriers photogenerated in the semiconductor or injected into the semiconductor. As discussed in Section 5.2, the observed spectra of *photogenerated* carriers in bare semiconductors can be explained by a band-like transport of electrons localized inside the semiconductor nanoparticles. The assumptions of our model of transient conductivity closely resemble those of the flight phase of the "random flight model" [93]. The Monte-Carlo simulations revealed that the probability p_r that an electron is reflected by the surface is 80% for ZnO and 90% for TiO$_2$ [11]. This means that long-range electron transport (relevant for the solar cell operation) indeed exists; however, it is considerably reduced due to the limited connectivity between the nanoparticles [94]. The difference between the spectra of ZnO and TiO$_2$ are mainly

related to the large difference in effective electron masses. The shape of the conductivity spectrum (i.e., namely the ratio between the real and imaginary part) is the same for carriers photogenerated in bare and sensitized nanoparticles. This means that attachment of neutral dye molecules does not influence the electron transport properties. Note that the magnitudes of THz conductivities both in bare and sensitized samples should be taken with care; since they are scaled by charge yields, they may be affected by inhomogeneities of the samples.

Apart from the amplitudes, the conductivity spectra of electrons *injected* into TiO$_2$ nanoparticles from either Ru-N3 or ZnTPP-Ipa are the same as the spectrum of *photogenerated* electrons in TiO$_2$. We thus conclude that dye molecules either in their neutral or oxidized state do not influence electron transport in TiO$_2$. The small variance in the zero crossing of the imaginary part of conductivity can be attributed to slightly different nanoparticle diameters and/or probabilities p_r in individual samples.

In contrast, the conductivity spectrum of electrons *injected* into ZnO differs from the spectrum of *photogenerated* electrons; namely, the real part of conductivity is considerably lower. Our hypothesis is that cations restrict the motion of injected electrons even after these escape from the EC complex. The interaction between the cations and the injected electrons is necessarily electrostatic. This interaction is screened in TiO$_2$ nanoparticles due to their high permittivity (80 compared to 8 in ZnO) so that the oxidized dye molecules do not influence electron transport in TiO$_2$, in agreement with our observations.

In order to confirm our hypothesis and to further understand the influence of oxidized dye molecules on the electron transport in ZnO, we investigated the response of electrons localized within the nanoparticles and moving in a model potential. The method from Section 5.2 was extended to account for the electron movement in a potential. For the sake of simplicity, we consider that the semiconductor nanoparticles are nanocubes surrounded by a border; the border properties are the same as those of the bare nanoparticles (namely the electron reflection probability p_r). The attractive electrostatic force is approximated using a harmonic potential. Its minimum is located at the nanoparticle surface (Fig. 16). The advantage of this configuration is that the low permeability (high p_r) of the nanoparticle surface mimics the repulsive force which prevents recombination in the real system. Under these conditions, the calculations match the experimental data if a harmonic potential with the eigenfrequency of 10 THz is used. This model is of course very approximate, nevertheless it shows that the height of the potential barrier for the electron transport is about 100 meV (see Fig. 16a). The degree of electron localization caused by the potential is illustrated by the electron distribution function plot in Fig. 16b.
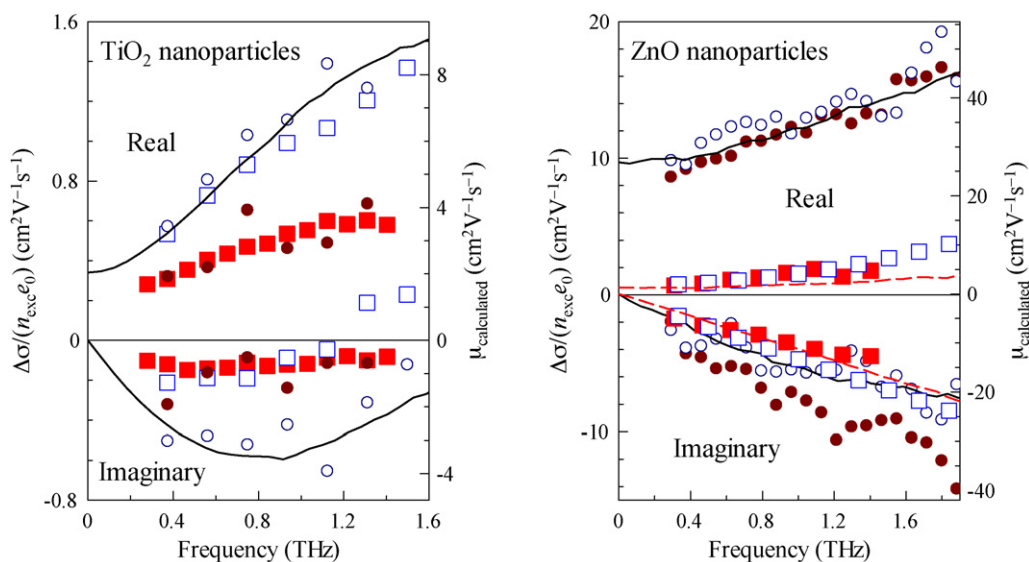
Sensitizer	Photogeneration		Injection	
	—	ZnTPP-Ipa	Ru-N3	ZnTPP-Ipa
Symbol	●	○	☐	■
Wavelength (nm)	300 (TiO$_2$) or 266 (ZnO)		400	558
Fluence (10^{14} ph/cm^2)	1 (TiO$_2$) or 0.7 (ZnO)		4	2
Pump-probe delay (ps)	20		300	

Fig. 15. Transient far-infrared conductivity spectra in bare and dye-sensitized ZnO and TiO$_2$ nanoparticles. Symbols (left axis): measured data; lines (right axis): calculated mobility of directly photogenerated electrons (solid) and injected electrons (dashed). These lines overlap in the left graph [after Ref. [83]].
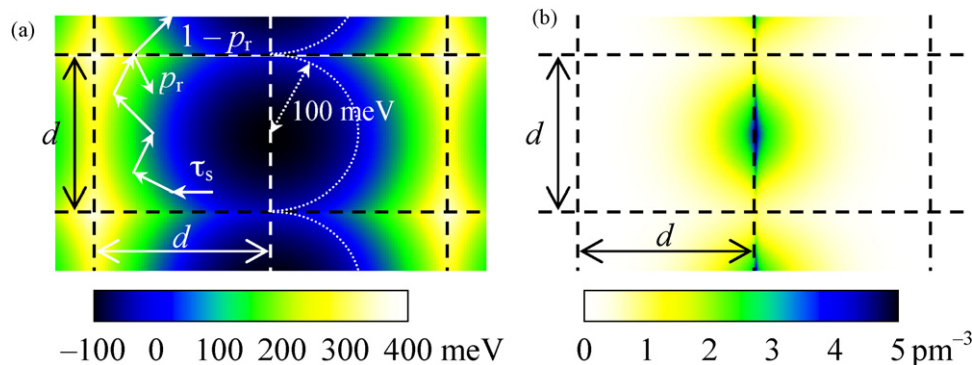
Fig. 16. (a) Geometry employed in the Monte-Carlo simulations of electrons interacting with dye cations. The cation is located in the center of the picture. The dashed lines indicate nanoparticle boundaries. (b) Calculated electron density distribution within the configuration sketched in (a) [after Ref. [83]].

7.3. Resulting picture

Electron injection into ZnO results in the formation of a bound electron–cation complex, which breaks up into an electron and cation or recombines on the time scale of tens to hundreds of picoseconds. The mobility of electrons that escape from the complex is strongly impaired by attractive electrostatic interaction with the cation at the semiconductor surface. In TiO$_2$, injection results in instantaneous formation of mobile electrons and the charge recombination is very slow. We attribute the different charge transport and recombination in the two semiconductors to the screening of the electrostatic interaction in TiO$_2$ due to its high dielectric permittivity. Direct photoexcitation of the semiconductor results in instantaneous formation of mobile electrons for both ZnO and TiO$_2$. Electrons also jump between particles with low probability.

ZnO is being explored as a promising material for many opto-electronics applications, including dye-sensitized solar cells, due to its ability to self assemble into various nanostructures and its high intrinsic electron mobility [95]. The EC complex formation in dye-sensitized materials, with its consequences of fast charge recombination and drastically reduced mobility could limit the use of ZnO as a solar cell material. On the other hand, these drawbacks can be possibly remedied by an improved technology of preparation, e.g., by coating the ZnO nanoparticles with a thin layer of a high dielectric permittivity material.

8. Summary

Time-resolved THz spectroscopy is a powerful non-contact method for investigation of the charge transport. Due to the high

frequency of the probing radiation, the photogenerated charges do not typically diffuse by more than a few tens of nanometers during one cycle of the probing radiation. The THz conductivity spectra thus provide information about transport on nanoscopic distances and contain rich fingerprints of charge transport mechanisms in nanostructured semiconductors. On the other hand, understanding these conductivity spectra remains a rather complex task. One major problem is how to describe the charge transport and corresponding spectra of THz conductivity. In the manuscript, we reviewed two prototypic examples: band-like transport of electrons localized in semiconductor nanoparticles, and hole hopping along polymer chains. Another major issue is due to the inherently inhomogeneous nature of nanostructures. That implies existence of depolarization fields which more or less dramatically influence the conductivity, depending on whether the photoconducting material is or is not percolated.

Acknowledgements

References

[1] M.A. Green, K. Emery, Y. Hishikawa, W. Warta, Solar cell efficiency tables (version 35), Prog. Photovolt.: Res. Appl. 18 (2010) 144–150.

[2] S.H. Park, A. Roy, S. Beaupré, S. Cho1, N. Coates, J.S. Moon, D. Moses, M. Leclerc, K. Lee, A.J. Heeger, Bulk heterojunction solar cells with internal quantum efficiency approaching 100%, Nat. Photon. 3 (2009) 297–302.

[3] V.I. Arkhipov, I.I. Fishchuk, A. Kadashchuk, H. Bässler, Charge transport in disordered organic semiconductors, in: G. Lanzani (Ed.), Photophysics of Molecular Materials, Wiley-VCH Verlag & Co. KGaA, Weinheim, 2006, pp. 261–366.

[4] P. Prins, F.C. Grozema, F. Galbrecht, U. Scherf, L.D.A. Siebbeles, Charge transport along coiled conjugated polymer chains, J. Phys. Chem. C 111 (2007) 11104–11112.

[5] J.B. Baxter, E.S. Aydil, Nanowire-based dye-sensitized solar cells, Appl. Phys. Lett. 86 (5) (2005) 3114.

[6] E. Galoppini, J. Rochford, H. Chen, G. Saraf, Y. Lu, A. Hagfeldt, G. Boschloo, Fast electron transport in metal organic vapor deposition grown dye-sensitized ZnO nanorod solar cells, J. Phys. Chem. B 110 (2006) 16159–21616.

[7] J.B. Baxter, C.A. Schmuttenmaer, Conductivity of ZnO nanowires, nanoparticles, and thin films using time-resolved terahertz spectroscopy, J. Phys. Chem. B 110 (2006) 25229–25239.

[8] F.A. Hegmann, O. Ostroverkhova, D.G. Cooke, Probing organic semiconductors with terahertz pulses, in: G. Lanzani (Ed.), Photophysics of Molecular Materials, Wiley-VCH Verlag & Co. KGaA, Weinheim, 2006, pp. 367–428.

[9] C.A. Schmuttenmaer, Exploring dynamics in the far-infrared with terahertz spectroscopy, Chem. Rev. 104 (2004) 1759–1779.

[10] D. Hertel, H. Bässler, Photoconduction in amorphous organic solids, Chem. Phys. Chem. 9 (2008) 666–688.

[11] H. Němec, P. Kužel, V. Sundström, Far-infrared response of free charge carriers localized in semiconductor nanoparticles, Phys. Rev. B 79 (11) (2009) 5309.

[12] T.J. Savenije, J.E. Kroeze, M.M. Wienk, J.M. Kroon, J.M. Warman, Mobility and decay kinetics of charge carriers in photoexcited PCBM/PPV blends, Phys. Rev. B 69 (15) (2004) 5205.

[13] J. Cabanillas-Gonzalez, T. Virgili, A. Gambetta, G. Lanzani, T.D. Anthopoulos, D.M. de Leeuw, Photoinduced transient Stark spectroscopy in organic semiconductors: a method for charge mobility determination in the picosecond regime, Phys. Rev. Lett. 96 (10) (2006) 6601.

[14] M.C. Beard, G.M. Turner, C.A. Schmuttenmaer, Subpicosecond carrier dynamics in low-temperature grown GaAs as measured by time-resolved terahertz spectroscopy, J. Appl. Phys. 90 (2001) 5915–5923.

[15] J.C. Delagnes, P. Mounaix, H. Němec, L. Fekete, F. Kadlec, P. Kužel, M. Martin, J. Mangeney, High photocarrier mobility in ultrafast ion-irradiated $In_{0.53}Ga_{0.47}As$ for terahertz applications, J. Phys. D.: Appl. Phys. 42 (19) (2009) 5103.

[16] S.L. Dexheimer, Terahertz Spectroscopy – Principles and Applications, CRC Press, Boca Raton, 2008.

[17] T.-I. Jeon, D. Grischkowsky, Nature of conduction in doped silicon, Phys. Rev. Lett. 78 (1997) 1106–1109.

[18] N.V. Smith, Classical generalization of the Drude formula for the optical conductivity, Phys. Rev. B 64 (15) (2001) 5106.

[19] G.M. Turner, M.C. Beard, C.A. Schmuttenmaer, Carrier localization and cooling in dye-sensitized nanocrystalline titanium dioxide, J. Phys. Chem. B 106 (2002) 11716–11719.

[20] X. Ai, M.C. Beard, K.P. Knutsen, S.E. Shaheen, G. Rumbles, R.J. Ellingson, Photoinduced charge carrier generation in a poly(3-hexylthiophene) and methanofullerene bulk heterojunction investigated by time-resolved terahertz spectroscopy, J. Phys. Chem. B 110 (2006) 25462–25471.

[21] H.-K. Nienhuys, V. Sundström, Influence of plasmons on terahertz conductivity measurements, Appl. Phys. Lett. 87 (1) (2005) 2101.

[22] J.C. Maxwell-Garnett, Colours in metal glasses and in metallic films, Philos. Trans. R. Soc. Lond. Ser. A 203 (1904) 385.

[23] D.A.G. Bruggeman, Berechnung verschiedener physikalischer Konstanten von heterogenen Substanzen, Ann. Phys. 416 (1935) 636.

[24] E. Hendry, M. Koeberg, B. O'Regan, M. Bonn, Local field effects on electron transport in nanostructured TiO_2 revealed by terahertz spectroscopy, Nano Lett. 6 (2006) 755–759.

[25] M.C. Beard, G.M. Turner, C.A. Schmuttenmaer, Size-dependent photoconductivity in CdSe nanoparticles as measured by time-resolved terahertz spectroscopy, Nano Lett. 2 (2002) 983–987.

[26] E. Hendry, J.M. Schins, L.P. Candeias, L.D.A. Siebbeles, M. Bonn, Efficiency of exciton and charge carrier photogeneration in a semiconducting polymer, Phys. Rev. Lett. 92 (19) (2004) 6601.

[27] J.C. Hummelen, B.W. Knight, F. LePeq, F. Wudl, J. Yao, C.L. Wilkins, Preparation and characterization of fulleroid and methanofullerene derivatives, J. Org. Chem. 60 (1995) 499–503.

[28] E. Hendry, M. Koeberg, J.M. Schins, H.K. Nienhuys, V. Sundström, L.D.A. Siebbeles, M. Bonn, Interchain effects in the ultrafast photophysics of a semiconducting polymer: THz time-domain spectroscopy of thin films and isolated chains in solution, Phys. Rev. B 71 (12) (2005) 5201.

[29] E. Hendry, M. Koeberg, J.M. Schins, L.D.A. Siebbeles, M. Bonn, Free carrier photogeneration in polythiophene versus poly(phenylene vinylene) studied with THz spectroscopy, Chem. Phys. Lett. 432 (2006) 441–445.

[30] P.D. Cunningham, L.M. Hayden, Carrier dynamics resulting from above and below gap excitation of P3HT and P3HT/PCBM investigated by optical-pump terahertz-probe spectroscopy, J. Phys. Chem. C 112 (2008) 7928–7935.

[31] P. Parkinson, J. Lloyd-Hughes, M.B. Johnston, L.M. Herz, Efficient generation of charges via below-gap photoexcitation of polymer–fullerene blend films investigated by terahertz spectroscopy, Phys. Rev. B 78 (11) (2008) 5331.

[32] O. Esenturk, R.J. Kline, D.M. Deongchamp, E.J. Heilweil, Conjugation effects on carrier mobilities of polythiophenes probed by time-resolved terahertz spectroscopy, J. Phys. Chem. C 112 (2008) 10587–10590.

[33] O. Esenturk, J.S. Melinger, E.J. Heilweil, Terahertz mobility measurements on poly-3-hexylthiophene films: device comparison, molecular weight, and film processing effects, J. Appl. Phys. 103 (2) (2008) 3102.

[34] H. Němec, H.-K. Nienhuys, F. Zhang, O. Inganäs, A. Yartsev, V. Sundström, Charge carrier dynamics in alternating polyfluorene copolymer:fullerene blends probed by terahertz spectroscopy, J. Phys. Chem. C 112 (2008) 6558.

[35] F.C. Grozema, P.Th. van Duijnen, Y.A. Berlin, M.A. Ratner, L.D.A. Siebbeles, Intramolecular charge transport along isolated chains of conjugated polymers: effect of torsional disorder and polymerization defects, J. Phys. Chem. B 106 (2002) 7791–7795.

[36] P.D. Cunningham, L.M. Hayden, H.-L. Yip, A.K.-Y. Jen, Charge carrier dynamics in metalated polymers investigated by optical-pump terahertz-probe spectroscopy, J. Phys. Chem. B 113 (2009) 15427–15432.

[37] H. Němec, H.-K. Nienhuys, E. Perzon, F. Zhang, O. Inganäs, P. Kužel, V. Sundström, Ultrafast conductivity in a low-band-gap polyphenylene and fullerene blend studied by terahertz spectroscopy, Phys. Rev. B 79 (24) (2009) 5326.

[38] F.A. Hegmann, R.R. Tykwinski, K.P.H. Lui, J.E. Bullock, J.E. Anthony, Picosecond transient photoconductivity in functionalized pentacene molecular crystals probed by terahertz pulse spectroscopy, Phys. Rev. Lett. 89 (22) (2002) 7403.

[39] O. Ostroverkhova, D.G. Cooke, S. Shcherbyna, R.F. Egerton, F.A. Hegmann, R.R. Tykwinski, J.E. Anthony, Bandlike transport in pentacene and functionalized pentacene thin films revealed by subpicosecond transient photoconductivity measurements, Phys. Rev. B 71 (3) (2005) 5204.

[40] V.K. Thorsmølle, R.D. Averitt, X. Chi, D.J. Hilton, D.L. Smith, A.P. Ramirez, A.J. Taylor, Ultrafast conductivity dynamics in pentacene probed using terahertz spectroscopy, Appl. Phys. Lett. 84 (2004) 891–893.

[41] F.C. Grozema, L.D.A. Siebbeles, Mechanisms of charge transport in self-organizing organic materials, Int. Rev. Phys. Chem. 27 (2008) 87–138.

[42] H.A. van Laarhoven, C.F.J. Flipse, M. Koeberg, M. Bonn, E. Hendry, G. Orlandi, O.D. Jurchescu, T.T.M. Palstra, A. Troisi, On the mechanism of charge transport in pentacene, J. Chem. Phys. 129 (4) (2008) 4704.

[43] M.C. Beard, G.M. Turner, J.E. Murphy, O.I. Micic, M.C. Hanna, A.J. Nozik, C.A. Schmuttenmaer, Electronic coupling in InP nanoparticle arrays, Nano Lett. 3 (2003) 1695–1699.

[44] J.E. Murphy, M.C. Beard, A.J. Nozik, Time-resolved photoconductivity of PbSe nanocrystal arrays, J. Phys. Chem. B 110 (2006) 25455–25461.

[45] D.G. Cooke, A.N. MacDonald, A. Hryciw, J. Wang, Q. Li, A. Meldrum, F.A. Hegmann, Transient terahertz conductivity in photoexcited silicon nanocrystal films, Phys. Rev. B 73 (2006) 193311.

[46] D.G. Cooke, A.N. MacDonald, A. Hryciw, A. Meldrum, J. Wang, Q. Li, F.A. Hegmann, Ultrafast terahertz conductivity of photoexcited nanocrystalline silicons, J. Mater. Sci.: Mater. Electron. 18 (2007) S447–S452.

[47] H. Ahn, Y.-P. Ku, Y.-C. Wang, C.-H. Chuang, S. Gwo, C.-L. Pan, Terahertz spectroscopic study of vertically aligned InN nanorods, Appl. Phys. Lett. 91 (16) (2007) 3105.

[48] M. Walther, D.G. Cooke, C. Sherstan, M. Hajar, M.R. Freeman, F.A. Hegmann, Terahertz conductivity of thin gold films at the metal-insulator percolation transition, Phys. Rev. B 76 (12) (2007) 5408.

[49] Z. Mics, P. Kužel, P. Jungwirth, S.E. Bradforth, Photoionization of atmospheric gases studied by time-resolved terahertz spectroscopy, Chem. Phys. Lett. 465 (2008) 20–24.

[50] P. Parkinson, J. Lloyd-Hughes, Q. Gao, H.H. Tan, C. Jagadish, M.B. Johnston, L.M. Herz, Transient terahertz conductivity of GaAs nanowires, Nano Lett. 7 (2007) 2162–2165.

[51] P. Parkinson, H.J. Joyce, Q. Gao, H.H. Tan, X. Zhang, J. Zou, C. Jagadish, L.M. Herz, M.B. Johnston, Carrier lifetime and mobility enhancement in nearly defect-free core–shell nanowires measured using time-resolved terahertz spectroscopy, Nano Lett. 9 (2009) 3349–3353.

[52] P.U. Jepsen, B.M. Fischer, A. Thoman, H. Helm, J.Y. Suh, R. Lopez, R.F. Haglund Jr., Metal-insulator phase transition in a VO_2 thin film observed with terahertz spectroscopy, Phys. Rev. B 74 (20) (2007) 5103.

[53] S.K.E. Merchant, J. Lloyd-Hughes, L. Sirbu, I.M. Tiginyanu, P. Parkinson, L.M. Herz, M.B. Johnston, Conductivity of nanoporous InP membranes investigated using terahertz spectroscopy, Nanotechnology 19 (39) (2008) 5704.

[54] J. Lloyd-Hughes, S.K.E. Merchant, L. Sirbu, I.M. Tiginyanu, M.B. Johnston, Tera-hertz photoconductivity of mobile electrons in nanoporous InP honeycombs, Phys. Rev. B 78 (8) (2008) 5320.

[55] J. Han, A.K. Azad, W. Zhang, Far-infrared characteristics of bulk and nanostruc-tured wide-bandgap semiconductors, J. Nanoelectron. Optoelectron. 2 (2007) 222–233.

[56] E. Hendry, M. Koeberg, F. Wang, H. Zhang, C. de Mello Donegá, D. Vanmaekel-bergh, M. Bonn, Direct observation of electron-to-hole energy transfer in CdSe quantum dots, Phys. Rev. Lett. 96 (5) (2006) 7408.

[57] F. Wang, J. Shan, M.A. Islam, I.P. Herman, M. Bonn, T.F. Heinz, Exciton polariz-ability in semiconductor nanocrystals, Nat. Mater. 5 (2006) 861–864.

[58] P. Prins, F.C. Grozema, J.M. Schins, L.D.A. Siebbeles, Frequency dependent mobil-ity of charge carriers along polymer chains with finite length, Phys. Stat. Sol. B 243 (2006) 382–386.

[59] P. Prins, F.C. Grozema, J.M. Schins, T.J. Savenije, S. Patil, U. Scherf, L.D.A. Siebbe-les, Effect of intermolecular disorder on the intrachain charge transport in ladder-type poly(p-phenylenes), Phys. Rev. B 73 (4) (2006) 5204.

[60] H. Scher, M. Lax, Stochastic transport in disordered solids, Phys. Rev. B 7 (1973) 4491–4502.

[61] O. Hilt, L.D.A. Siebbeles, Time and frequency dependent charge carrier mobil-ity of one-dimensional chains with energetic disorder, Chem. Phys. Lett. 269 (1997) 257–262.

[62] R. Kubo, Statistical–mechanical theory of irreversible processes, J. Phys. Soc. Jpn. 12 (1957) 570–586.

[63] H. Němec, P. Kužel, F. Kadlec, D. Fattakhova-Rohlfing, J. Szeifert, T. Bein, V. Kalousek, J. Rathouský, Ultrafast terahertz photoconductivity in nanocrys-talline mesoporous TiO_2 films, Appl. Phys. Lett. 96 (6) (2010) 2103.

[64] J.M. Szeifert, D. Fattakhova-Rohlfing, D. Georgiadou, V. Kalousek, J. Rathouský, D. Kuang, S. Wenger, S.M. Zakeeruddin, M. Grätzel, T. Bein, "Brick and mortar" strategy for the formation of highly crystalline mesoporous titania films from nanocrystalline building blocks, Chem. Mater. 21 (2009) 1260–1265.

[65] L. Fekete, P. Kužel, H. Němec, F. Kadlec, A. Dejneka, J. Stuchlík, A. Fejfar, Ultrafast carrier dynamics in microcrystalline silicon probed by time-resolved terahertz spectroscopy, Phys. Rev. B 79 (11) (2009) 5306.

[66] J. Kočka, H. Stuchlíková, J. Stuchlík, B. Rezek, T. Mates, V. Švrček, I. Pelant, A. Fej-far, Model of transport in microcrystalline silicon, J. Noncryst. Solids 299–302 (2002) 355–359.

[67] E. Perzon, F. Zhang, M. Andersson, W. Mammo, O. Inganäs, M.R. Andersson, A conjugated polymer for near infra red optoelectronic applications, Adv. Mater. 19 (2007) 3308–3311.

[68] O. Inganäs, M. Svensson, F. Zhang, A. Gadisa, N.K. Persson, X. Wang, M.R. Ander-sson, Low bandgap alternating polyfluorene copolymers in plastic photodiodes and solar cells, Appl. Phys. A 79 (2004) 31–35.

[69] S. De, T. Pascher, M. Maiti, K.G. Jespersen, T. Kesti, F. Zhang, O. Inganäs, A. Yart-sev, V. Sundström, Geminate charge recombination in alternating polyfluorene copolymer/fullerene blends, J. Am. Chem. Soc. 129 (2007) 8466–8472.

[70] I.G. Scheblykin, A. Yartsev, T. Pullerits, V. Gulbinas, V. Sundström, Excited state and charge photogeneration dynamics in conjugated polymer, J. Phys. Chem. B 111 (2007) 6303–6321.

[71] C.J. Brabec, G. Zerza, G. Cerullo, S. De Silvestri, S. Luzzati, J.C. Hummelen, S. Sariciftci, Tracing photoinduced electron transfer process in conjugated poly-mer/fullerene bulk heterojunctions in real time, Chem. Phys. Lett. 340 (2001) 232–236.

[72] H. Němec, F. Kadlec, P. Kužel, Methodology of an optical pump–terahertz probe experiment: an analytical frequency-domain approach, J. Chem. Phys. 117 (2002) 8454–8466.

[73] P. Kužel, F. Kadlec, H. Němec, Propagation of terahertz pulses in photoexcited media: analytical theory for layered systems, J. Chem. Phys. 127 (2) (2007) 4506.

[74] S.K. Pal, T. Kesti, M. Maiti, F. Zhang, O. Inganäs, S. Hellström, M.R. Andersson, F. Oswald, F. Langa, T. Österman, T. Pascher, A. Yartsev, V. Sundström, Gemi-nate charge recombination in polymer/fullerene bulk heterojunction films and implications for solar cell function, J. Am. Chem. Soc. 132 (2010) 12440–12451.

[75] G. Benkö, J. Kallioinen, J.E.I. Korppi-Tommola, A.P. Yartsev, V. Sundström, Photoinduced ultrafast dye-to-semiconductor electron injection from nonther-malized and thermalized donor states, J. Am. Chem. Soc. 124 (2002) 489–493.

[76] S. Ardo, G.J. Meyer, Photodriven heterogeneous charge transfer with transition-metal compounds anchored to TiO_2 semiconductor surfaces, Chem. Soc. Rev. 38 (2009) 115–164.

[77] R. Katoh, A. Furube, A.V. Barzykin, H. Arakawa, M. Tachiya, N.A. Anderson, T. Lian, Kinetics and mechanism of electron injection and charge recombination in dye-sensitized nanocrystalline semiconductors, Coord. Chem. Rev. 248 (2004) 1195–1213.

[78] N.A. Anderson, T. Lian, Ultrafast electron transfer at the molecule–semiconductor nanoparticle interface, Annu. Rev. Phys. Chem. 56 (2005) 491–519.

[79] G. Benkö, P. Myllyperkiö, J. Pan, A.P. Yartsev, V. Sundström, Photoinduced elec-tron injection from $Ru(dcbPY)_2(NCS)_2$ to SnO_2 and TiO_2 nanocrystalline films, J. Am. Chem. Soc. 125 (2003) 1118–1119.

[80] G. Benkö, J. Kallioinen, P. Myllyperkiö, F. Trif, J.E.I. Korppi-Tommola, A.P. Yart-sev, V. Sundström, Interligand electron transfer determines triplet excited state electron injection in RuN3-sensitized TiO_2 films, J. Phys. Chem. B 108 (2004) 2862–2867.

[81] P. Tiwana, P. Parkinson, M.B. Johnston, H.J. Snaith, L.M. Herz, Ultrafast terahertz conductivity dynamics in mesoporous TiO_2: influence of dye sensitization and surface treatment in solid-state dye-sensitized solar cells, J. Phys. Chem. C 114 (2010) 1365–1371.

[82] S.G. Abuabara, C.W. Cady, J.B. Baxter, C.A. Schmuttenmaer, R.H. Crabtree, G.W. Brudvig, V.S. Batista, Ultrafast photooxidation of Mn^{II}-terpyridine com-plexes covalently attached to TiO_2 nanoparticles, J. Phys. Chem. C 111 (2007) 11982–11990.

[83] H. Němec, J. Rochford, O. Taratula, E. Galoppini, P. Kužel, T. Polívka, A. Yartsev, V. Sundström, Impact of electron–cation interaction on electron mobility in dye-sensitized ZnO and TiO_2 nanocrystals, Phys. Rev. Lett. 104 (19) (2010) 7401.

[84] J. Rochford, E. Galoppini, Zinc(II) tetraarylporphyrins anchored to TiO_2, ZnO, and ZrO_2 nanoparticle films through rigid-rod linkers, Langmuir 24 (2008) 5366–5374.

[85] M.K Nazeeruddin, A. Kay, I. Rodicio, R. Humphry-Baker, E. Müller, P. Liska, N. Vlachopoulos, M. Grätzel, Conversion of light to electricity by cis-X_2bis(2,2′-bipyridyl-4,4′-dicarboxylate)ruthenium(II) charge-transfer sensitizers (X = Cl^-, Br^-, I^-, CN^-, and SCN^-) on nanocrystalline titanium dioxide electrodes, J. Am. Chem. Soc. 115 (1993) 6382–6390.

[86] K.G. Jespersen, F. Zhang, A. Gadisa, V. Sundström, A. Yartsev, O. Inganäs, Charge formation and transport in bulk-heterojunction solar cells based on alternat-ing polyfluorene copolymers blended with fullerenes, Org. Electron. 7 (2006) 235–242.

[87] J.B. Asbury, E. Hao, Y. Wang, H.N. Ghosh, T. Lian, Ultrafast electron transfer dynamics from molecular adsorbates to semiconductor nanocrystalline thin films, J. Phys. Chem. B 105 (2001) 4545–4557.

[88] S. Aono, I. Okura, A. Yamada, Photoinduced electron transfer between $Zn(TPPS)_3^{3-}$ and viologens, J. Phys. Chem. 89 (1985) 1593–1598.

[89] Y. Tachibana, S.A. Haque, I.P. Mercer, J.R. Durrant, D.R. Klug, Electron injection and recombination in dye sensitized nanocrystalline titanium dioxide films: a comparison of ruthenium bipyridyl and porphyrin sensitizer dyes, J. Phys. Chem. B 104 (2000) 1198–1205.

[90] J.E. Rogers, K.A. Nguyen, D.C. Hufnagle, D.G. McLean, W. Su, K.M. Gossett, A.R. Burke, S.A. Vinogradov, R. Pachter, P.A. Fleitz, Observation and interpretation of annulated porphyrins: studies on the photophysical properties of meso-tetraphenylmetalloporphyrins, J. Phys. Chem. A 107 (2003) 11331–11339.

[91] J. Larsen, B. Brüggemann, T. Polívka, V. Sundström, E. Åkesson, Energy trans-fer within Zn-porphyrin dendrimers: study of the singlet–singlet annihilation kinetics, J. Phys. Chem. A 109 (2005) 10654–10662.

[92] A. Furube, R. Katoh, K. Hara, S. Murata, H. Arakawa, M. Tachiya, Ultrafast stepwise electron injection from photoexcited Ru-complex into nanocrys-talline ZnO film via intermediates at the surface, J. Phys. Chem. B 107 (2003) 4162–4166.

[93] A.V. Barzykin, M. Tachiya, Mechanism of charge recombination in dye-sensitized nanocrystalline semiconductors: random flight model, J. Phys. Chem. B 106 (2002) 4356–4363.

[94] M.J. Cass, F.L. Qiu, A.B. Walker, A.C. Fisher, L.M. Peter, Influence of grain mor-phology on electron transport in dye sensitized nanocrystalline solar cells, J. Phys. Chem. B 107 (2003) 113–119.

[95] C. Klingshirn, ZnO: from basics towards applications, Phys. Stat. Sol. B 244 (2007) 3027–3073.